

A study on the Clustering Properties of Radio-Selected sources in the Lockman Hole Region at 325 MHz

Aishrila Mazumder,¹★ Arnab Chakraborty,^{1,2,3} Abhirup Datta¹

¹*Department of Astronomy, Astrophysics and Space Engineering, Indian Institute of Technology Indore, Indore 453552, India*

²*Department of Physics, McGill University, 3600 rue University, Montreal, QC H3A 2T8, Canada*

³*McGill Space Institute, McGill University, 3550 rue University, Montreal, QC H3A 2A7, Canada*

Accepted XXX. Received YYY; in original form ZZZ

ABSTRACT

Studying the spatial distribution of extragalactic source populations is vital in understanding the matter distribution in the Universe. It also enables understanding the cosmological evolution of dark matter density fields and the relationship between dark matter and luminous matter. Clustering studies are also required for EoR foreground studies since it affects the relevant angular scales. This paper investigates the angular and spatial clustering properties and the bias parameter of radio-selected sources in the Lockman Hole field at 325 MHz. The data probes sources with fluxes ≥ 0.3 mJy within a radius of 1.8° around the phase center of a $6^\circ \times 6^\circ$ mosaic. Based on their radio luminosity, the sources are classified into Active Galactic Nuclei (AGNs) and Star-Forming Galaxies (SFGs). Clustering and bias parameters are determined for the combined populations and the classified sources. The spatial correlation length and the bias of AGNs are greater than SFGs- indicating that more massive haloes host the former. This study is the first reported estimate of the clustering property of sources at 325 MHz, intermediate between the preexisting studies at high and low-frequency bands. It also probes a well studied deep field at an unexplored frequency with moderate depth and area. Clustering studies require such observations along different lines of sight, with various fields and data sets across frequencies to avoid cosmic variance and systematics. Thus, an extragalactic deep field has been studied in this work to contribute to this knowledge.

Key words: Galaxies - galaxies: active< Galaxies- cosmology: large-scale structure of Universe<Cosmology - cosmology: observations<Cosmology - radio continuum: galaxies< Resolved and unresolved sources as a function of wavelength

1 INTRODUCTION

Observations of the extragalactic sky at radio frequencies are essential for the study of both large-scale structures (LSS) and different populations of sources present in the Universe. The initial research on LSS using clustering was performed with the reporting of slight clustering signals from nearby sources (Seldner & Peebles 1981; Shaver & Pierre 1989). With the advent of large-area surveys like FIRST (Faint Images of the Radio Sky at Twenty-Centimeters, Becker et al. 1995) and NVSS (NRAO VLA Sky Survey, Condon et al. 1998), the studies became more precise due to the large number of sources detected in these surveys.

The extragalactic sky at radio frequencies is dominated by sources below mJy flux densities (at frequencies from MHz to a few GHz, see for example Simpson et al. 2006; Mignano, A. et al. 2008; Seymour et al. 2008; Smolčić et al. 2008; Prandoni et al. 2018). The source population can be divided into Active Galactic Nuclei

(AGNs) and Star-Forming Galaxies (SFGs) (Condon 1989; Afonso et al. 2005; Simpson et al. 2006; Bonzini et al. 2013; Padovani et al. 2015; Vernstrom et al. 2016). The dominant sources at these fluxes are SFGs, AGNs of Fanaroff-Riley type I (FR I, Fanaroff & Riley 1974), and radio-quiet quasars (Padovani 2016). Emission mechanism dominating populations at low frequencies (≤ 10 GHz) is synchrotron emission, modeled as a power law of the form $S_\nu \propto \nu^{-\alpha}$, where α is the spectral index. Study of the extragalactic population using synchrotron emission can help trace the evolution of the LSS in the Universe. It also helps to map their dependence on various astrophysical and cosmological parameters (Blake & Wall 2002b; Lindsay et al. 2014; Hale et al. 2018). Radio continuum surveys, both wide and deep, help constrain the overall behavior of cosmological parameters and study their evolution and relation to the environment (Best & Heckman 2012; Ineson et al. 2015; Hardcastle et al. 2016; Calistro Rivera et al. 2017; Williams et al. 2018). The clustering pattern of radio sources (AGNs and SFGs) can be studied to analyze the evolution of matter density distribution. Clustering measurements for these sources also provide a tool for tracing the

★ E-mail: aishri0208@gmail.com

underlying dark matter distribution (Press & Schechter 1974; Lacey & Cole 1993, 1994; Sheth & Tormen 1999; Mo et al. 2010). The distribution of radio sources derived from clustering is related to the matter power spectrum and thus provides insights for constraining cosmological parameters that define the Universe. The relationship of the various galaxy populations with the underlying dark matter distribution also helps assess the influence of the environment on their evolution. Clustering studies are also required for extragalactic foreground characterization for EoR and post-EoR science. Spatial clustering of extragalactic sources with flux density greater than the sub-mJy range (around ~ 150 MHz) dominate fluctuations at angular scales of arcminute range. Thus, their modeling and removal allow one to detect fluctuation of the 21-cm signal on the relevant angular scales.

The definition of clustering is the probability excess above a certain random distribution (taken to be Poisson for astrophysical sources) of finding a galaxy within a certain scale of a randomly selected galaxy. This is known as the two-point correlation function (Peebles 1980). The angular two-point correlation function has been studied in optical surveys like the 2dF Galaxy Redshift Survey (Peacock et al. 2001; Percival et al. 2001; Norberg et al. 2001), Sloan Digital Sky Survey (Eisenstein et al. 2005; Wang et al. 2013; de Simoni et al. 2013; Shi et al. 2016; Carvalho et al. 2016) and the Dark Energy Survey (Camacho et al. 2019). Optical surveys provide redshift information for sources either through photometry or spectroscopy. This information can be used to obtain the spatial correlation function and the bias parameter (Ross et al. 2007; Heinis et al. 2009; Salazar-Albornoz et al. 2017). But for optical surveys, observations of a large fraction of the sky is expensive in terms of cost and time. Additionally, optical surveys suffer the limitation of being dust-obscured for high redshift sources. However, at radio wavelengths, the incoming radiation from these sources do not suffer dust attenuation and thus can be used as a mean to probe such high z sources (Hao et al. 2011; Cucciati et al. 2012; Singh et al. 2014; Jarvis et al. 2016; Saxena et al. 2017). The highly sensitive radio telescopes like GMRT (Swarup et al. 1991), ASKAP (DeBoer et al. 2009), LOFAR (van Haarlem, M. P. et al. 2013) are also able to survey larger areas of the sky significantly faster. They are thus efficient for conducting large-area surveys in lesser time than the old systems while detecting lower flux densities. Therefore, radio surveys provide an efficient method for investigation of the clustering for the different AGN populations. Additionally, at low-frequencies ($\lesssim 1.4$ GHz), synchrotron radiation from SFGs provide insight into their star-formation rates (Bell 2003; Jarvis et al. 2010; Davies et al. 2016; Delhaize et al. 2017; Gürkan et al. 2018). These insights have lead to clustering studies of SFGs as well at low frequencies (Magliocchetti et al. 2017; Chakraborty et al. 2020). Through clustering studies of radio sources, deep radio surveys help trace how the underlying dark matter distribution is traced by luminous matter distribution. In addition to this, the two-point correlation functions can also provide other information relevant for cosmology by fitting parameterized models to the data to obtain acceptable ranges of parameters. These include the bias parameter, dark energy equations of state, and Ω_m (total density of matter), to name a few (Peebles 1980; Camera et al. 2012; Raccanelli et al. 2012; Planck Collaboration et al. 2014; Allison et al. 2015).

Extensive observations at multiple frequencies can help understand the relationship of the various source populations with their host haloes and individual structures (stars) present. It has been inferred from clustering observations that AGNs are primarily hosted in more massive haloes than SFGs and are also more strongly clustered (Gilli et al. 2009; Donoso et al. 2014; Magliocchetti et al.

2017; Hale et al. 2018). While AGNs are more clustered than SFGs, for the latter, the clustering appears to be dependent on the rate of star formation. SFGs with higher star formation rates are more clustered than the ones with a lower rate (since star formation rate is correlated to stellar mass, which in turn is strongly correlated to the mass of the host halo, see Magnelli et al. (2015); Delvecchio et al. (2021); Bonato et al. (2021) and references therein). Studying the large-scale distribution of dark matter by studying the clustering pattern of luminous baryonic matter is vital for understanding structure formation. From linear perturbation theory, galaxies are "biased" tracers of the underlying matter density field since they are mostly formed at the peak of the matter distribution (Peebles 1980). Bias parameter (b) traces the relationship between overdensity of a tracer δ and the underlying dark matter overdensity (δ_{DM}), given by $\delta = b\delta_{DM}$. The linear bias parameter is the ratio between the dark matter correlation function and the galaxy correlation function (Peebles (1980); Kaiser (1984); Bardeen et al. (1986), also see Desjacques et al. (2018) for a recent review). Measurement of the bias parameter from radio surveys will allow measurements which probe the underlying cosmology governing the LSS, and probe dark energy, modified gravity, and non-Gaussianity of the primordial density fluctuations (Blake et al. 2004; Carilli & Rawlings 2004; Seljak 2009; Raccanelli et al. 2015; Abdalla et al. 2015).

Analysis of the clustering pattern for extragalactic sources is also important for observations targeting the 21-cm signal of neutral hydrogen (HI) from the early Universe. These weak signals from high redshifts have their observations hindered by many orders of magnitude brighter foregrounds - namely diffuse galactic synchrotron emission (Shaver et al. 1999), free-free emission from both within the Galaxy as well as extragalactic sources (Cooray & Furlanetto 2004), faint radio-loud quasars (Matteo et al. 2002) and extragalactic point sources (Di Matteo et al. 2004). Di Matteo et al. (2004) showed that spatial clustering of extragalactic sources with flux density ≥ 0.1 mJy at 150 MHz (the equivalent flux density at 325MHz is ~ 0.05 mJy) dominate fluctuations at angular scale $\theta \gtrsim 1'$. Thus, their modeling and removal allow one to detect fluctuation of the 21-cm signal on relevant angular scales. So their statistical modeling is necessary to understand and quantify the effects of bright foregrounds. Many studies have modeled the extragalactic source counts as single power-law or smooth polynomial (Intema et al. 2017; Franzen et al. 2019) and the spatial distribution of sources as Poissonian (Ali et al. 2008) or having a simple power-law clustering. However, a Poisson distribution of foreground sources is very simplistic and may affect signal recovery for sensitive observations like those targeting the EoR signal (Ali et al. 2008; Trott et al. 2016). Thus more observations are required for low-frequency estimates of the clustering pattern of compact sources.

A number of studies have been done in recent years for observational determination of the clustering of radio selected sources (for instance Cress et al. (1996); Overzier et al. (2003); Lindsay et al. (2014); Magliocchetti et al. (2017); Hale et al. (2018, 2019); Rana & Bagla (2019); Chakraborty et al. (2020); Siewert et al. (2020)). However, more such studies are required for modeling the influence of different processes on the formation and evolution of LSS in the Universe. The sample used for such analyses should not be limited to small deep fields, since the limited number of samples makes clustering studies of different populations (AGNs/ SFGs) sample variance limited. Studies on the statistics of the source distribution are also essential for understanding the matter distribution across space. Thus, observations using sensitive instruments are required to conduct more detailed studies. At 1.4 GHz and above, many clustering studies are present (for instance Cress et al. (1996); Overzier

et al. (2003); Lindsay et al. (2014); Magliocchetti et al. (2017); Hale et al. (2018); Bonato et al. (2020)); however there extensive studies at low frequencies (and wider areas) are still required. The TIFR GMRT Sky Survey (TGSS) (Intema et al. 2017) is a wide-area survey of the northern sky at 150 MHz. But the available catalog from the TGSS- Alternate Data Release (TGSS-ADR) suggests that the data is systematics limited. Thus it is unsuitable for large-scale clustering measurements (Tiwari et al. 2019). The ongoing LOFAR Two-metre Sky Survey (LoTSS Shimwell, T. W. et al. 2017) at a central frequency of 144 MHz is expected to have very high sensitivity and cover a very wide area and thus provide excellent data for studying source distribution statistics at low frequencies (Siewert et al. 2020). However, to constrain cosmological parameters, consensus for the overall behavior of sources along different lines of sight and across frequencies is also required, and there data sets like the one analyzed here become important (Blake et al. 2004; Carilli & Rawlings 2004; Norris et al. 2013). Radio data has the advantage that even flux-limited samples contain high- z sources (Dunlop & Peacock 1990). Thus, using the entire radio band provides insights into physical processes driving the evolution of different galaxy populations and helps create a coherent picture of the matter distribution in the Universe. Therefore, studies at radio frequencies would help constrain the cosmology underlying structure formation and evolution.

The recent study of the clustering of the ELAIS-N1 field centered at 400 MHz using uGMRT by Chakraborty et al. (2020) was extremely sensitive, with an RMS (σ_{400})¹ of $15 \mu\text{Jy beam}^{-1}$. But the area covered was significantly smaller ($\sim 1.8 \text{ deg}^2$) than this work. This smaller field of view makes measurement of clustering properties on large angular scales impossible. Smaller areas also lead to smaller sample sizes for statistics, resulting in studies limited by cosmic variance. Another study of the HETDEX spring field at 144 MHz (using the data release 1 of LOFAR Two meter Sky Survey) by Siewert et al. (2020) has a sky coverage of ~ 350 square degree, but the mean σ_{150} is $\sim 91 \mu\text{Jy beam}^{-1}$. However, despite the sensitivity achieved in the survey, the analysis by Siewert et al. (2020) is limited to flux densities above 2 mJy. Motivated by the requirement for a study in the intermediate range (in terms of flux density, area covered, and frequency), this work aims to quantify the clustering of the sources detected in the Lockman Hole field. The data analyzed here fall in the intermediate category, with a survey area $\sim 6 \text{ deg}^2$ with $\sigma_{325} \sim 50 \mu\text{Jy beam}^{-1}$. It is thus ideal for clustering studies with a sizeable area of the sky covered (thus large angular scales can be probed) and moderately deep flux threshold (catalogue will have fluxes reliable to a lower value). Additionally, the Lockman Hole region has excellent optical coverage through surveys like SDSS and SWIRE; thus, associated redshift information is available to study spatial clustering and bias parameters. This frequency also has the additional advantage of having lesser systematics than the 150 MHz band while still being sensitive to the low-frequency characteristics of sources. New data releases for the LoTSS surveys promise greater sensitivity and source characterization over various deep fields targeted by these observations (Shimwell, T. W. et al. 2019; Tasse et al. 2021); all these observational data at multiple frequencies will put more precise constraints on the various parameters governing the structure formation and evolution.

This work uses archival GMRT data at 325 MHz covering a

field of view of $6^\circ \times 6^\circ$ through multiple pointings. In Mazumder et al. (2020), data reduction procedure is described in detail. This work used the source catalogue obtained there for clustering analyses. However, the entire dataset could not be used due to limiting residual systematics at large angular scales. The clustering pattern and linear bias parameter are determined for the whole population and sub-populations, i.e., AGNs and SFGs, separately. The previous work by Mazumder et al. (2020) had determined the flux distribution of sources (i.e., differential source count) and characterized the spatial property and the angular power spectrum of the diffuse galactic synchrotron emission using the same data.

This paper is arranged in the following manner: In section 2, a brief outline of the radio data as well as various optical data used is discussed; the classification into source sub-populations is also using radio luminosity of sources is also shown. The following section, i.e., Section 3 shows the clustering quantification - both in spatial and angular scales and calculation of linear bias for all the detected sources. Section 4 discusses the clustering property and bias for classified population, with a brief discussion on the choice of the field of view for this analysis discussed in Section 5. Finally, the paper is concluded in Section 6.

For this work, the best fitting cosmological parameters obtained from the Planck 2018 data (Planck Collaboration et al. 2019) has been used. The values are $\Omega_M = 0.31$, $\Omega_\Lambda = 0.68$, $\sigma_8 = 0.811$, & $H_0 = 67.36 \text{ km s}^{-1} \text{ Mpc}^{-1}$. The spectral index used for scaling the flux densities between frequencies is taken as $\alpha=0.8$.

2 OBSERVATIONS AND SOURCE CATALOGUES

This work uses 325 MHz GMRT archival data of the Lockman Hole region. The details of the data reduction procedure have been described in Mazumder et al. (2020), here it is discussed very briefly. The data were reduced using the SPAM pipeline (Intema et al. 2009; Intema 2014; Intema et al. 2017), which performs direction-independent as well as direction-dependent calibration techniques. The observation had 23 separate pointings, centered at ($\alpha_{2000} = 10^h 48^m 00^s$, $\delta_{2000} = 58^\circ 08' 00''$), each of which was reduced separately. The final image is a $6^\circ \times 6^\circ$ mosaic having off-source RMS of $50 \mu\text{Jy beam}^{-1}$ at the central frequency. Figure 1 shows the primary beam corrected final mosaic image of the observed region. This image was used to extract a source catalogue using Python Blob Detection and Source Finder² (PyBDSF, Mohan & Rafferty (2015)) above a minimum flux density $S_{325}^{\text{cut}} 0.3 \text{ mJy}$ (i.e., above $6\sigma_{325}$). A total of 6186 sources were detected and cataloged. The readers are referred to Mazumder et al. (2020) for details on catalogue creation and subsequent comparison with previous observations.

The redshift information for the sources are derived by matching with optical data from the Sloan Digital Sky Survey (SDSS)³ and the Herschel Extragalactic Legacy Project (HELP)^{4,5} (Shirley et al. 2019). The SDSS (York et al. 2000; Eisenstein et al. 2011) has been mapping the northern sky in the form of optical images as well as optical and near-infrared spectroscopy since 1998. The latest data release (DR16) is from the fourth phase of the survey

¹ Unless otherwise stated, $\sigma_{\text{frequency}}$ is the RMS sensitivity at the quoted frequency throughout the text.

² <https://www.astron.nl/citt/pybdsf/>

³ <https://www.sdss.org/>

⁴ <http://herschel.sussex.ac.uk/>

⁵ <https://github.com/H-E-L-P>

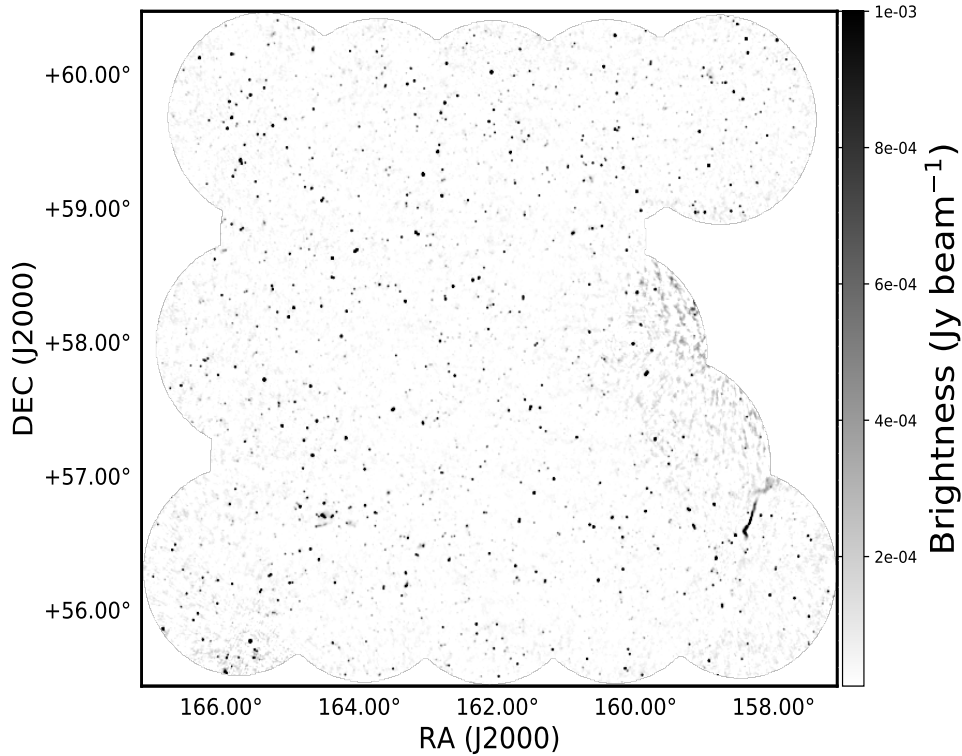


Figure 1. Primary beam corrected mosaic of the Lockman Hole region at 325 MHz. The off source RMS at the center is $\sim 50 \mu\text{Jy beam}^{-1}$ and beam size is $9.0'' \times 9.0''$. This image is a reproduction of Figure 1 of Mazumder et al. (2020)

(SDSS-IV, Blanton et al. (2017)). It includes the results for various survey components like the extended Baryon Oscillation Spectroscopic Survey eBOSS, SPectroscopic identification of ERosita Sources SPIDERS, Apache Point Observatory Galaxy Evolution Experiment 2 APOGEE-2, etc. The surveys have measured redshifts of a few million galaxies and have also obtained the highest precision value of the Hubble parameter $H(z)$ to date (Alam et al. 2021). An SQL query was run in the CasJobs⁶ server to obtain the optical data corresponding to the radio catalogue, and the catalogue thus obtained was used for further analysis.

HELP has produced optical to near-infrared astronomical catalogues from 23 extragalactic fields, including the Lockman Hole field. The final catalogue consists of ~ 170 million objects obtained from the positional cross-match with 51 surveys (Shirley et al. 2019). The performance of various templates and methods used for getting the photometric redshift is described in Duncan et al. (2017, 2018). Each of the individual fields is provided separate database in the *Herschel Database in Marseille* site⁷ where various products, field-wise and category wise are made available via "data management unit (DMU)". For the Lockman Hole field, the total area covered by various surveys is 22.41 square degrees with 1377139 photometric redshift objects. The Lockman Hole field is covered well in the Spitzer Wide-area InfraRed Extragalactic Legacy Survey (SWIRE) with photometric redshifts obtained as discussed in Rowan-Robinson et al. (2008, 2012). However, additional data from other survey catalogues like Isaac Newton Telescope - Wide Field Camera (INT-WFC, Lewis et al. (2000)), Red Cluster Sequence

Lensing Survey (RCSLenS, Hildebrandt et al. (2016)) catalogues, Panoramic Survey Telescope and Rapid Response System 3pi Steradian Survey (PanSTARRS-3SS, Chambers et al. (2019)), Spitzer Adaptation of the Red-sequence Cluster Survey (SpARCS, Muzzin et al. (2007)), UKIRT Infrared Deep Sky Survey - Deep Extragalactic Survey (UKIDSS-DXS, Lawrence et al. (2007)), Spitzer Extragalactic Representative Volume Survey (SERVS, Mauduit et al. (2012)) and UKIRT Hemisphere Survey (UHS, Dye et al. (2017)) resulted in more sources being detected and better photometric determination. The publicly available photometric catalogue for the Lockman Hole region was used to determine the redshift information for matched sources. The source catalogue derived from the 325 MHz observation is pre-processed, matched to add redshift information, and then further analysis is done. The following subsections describe these steps in detail.

2.1 Merging multi-component sources

The final map produced has a resolution of $9''$. The source finder might resolve an extended source into multiple components for such high-resolution maps. Such sources are predominantly radio galaxies that have a core at the center and hotspots that extend along the direction of the jet(s) or at their ends; these structures may be classified as separate sources (Magliocchetti et al. 1998; Prandoni et al. 2018; Williams, W. L. et al. 2019; Galvin et al. 2020). Using the NVSS catalogue, it has been shown in Blake & Wall (2002a) that large radio sources with unmarked components can significantly alter clustering measurements. Thus, for unbiased estimation of source clustering, such sources need to be identified and merged properly. A strong correlation between the angular extent of radio

⁶ <https://skyserver.sdss.org/casjobs/>

⁷ <https://hedam.lam.fr/HELP/>

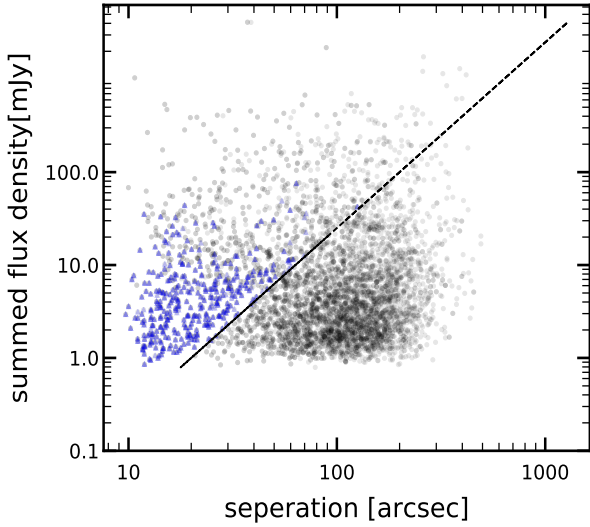


Figure 2. Sum of nearest neighbour flux densities from the 325 MHz catalogue as a function of separation between nearest neighbours in the catalogue are shown by light blue circles. Sources above the black dotted line (having an angular separation less than θ_{\max}) shown by blue triangles have their flux densities differing by a less than a factor of 4.

sources and their fluxes has been discovered by Oort (1987). The angular extent (θ) of a source is related to its flux density (S) by the θ -S relation, $\theta \propto \sqrt{S}$. This relation was used to identify resolved components of multi-component sources in surveys like the FIRST survey (Magliocchetti et al. 1998).

Identification of multi-component sources in the Lockman Hole catalogue resolved as separate sources are made using two criteria. The maximum separation between pairs of sources (using the θ -S relation) is given by $\theta_{\max} = 20\sqrt{S_{\text{total}}}$, where S_{total} is the summed flux of the source pairs (Huynh et al. 2005; Prandoni et al. 2018; Chakraborty et al. 2020). Sources identified by the above criteria have been considered as the same source if their flux densities differ by less than a factor of 4 (Huynh et al. 2005).

Figure 2 shows the separation between the nearest neighbour pairs from the 325 MHz catalogue as a function of the separation between them. Above the black dotted line, the sources have separation less than θ_{\max} as mentioned above. Blue triangles are sources that have flux density differences less than a factor of 4. The two criteria mentioned gave a sample of 683 sources (out of 6186 total) to have two or more components. After merging multi-component sources and filtering out random associations, 5489 sources are obtained in the revised catalogue. The position of the merged sources are the flux weighted mean position for their components.

2.2 Adding Redshift Information

As already mentioned, optical cross-identification have for the sources detected has been done using the HELP and SDSS catalogues. A positional cross-match with $9''$ matching radius (which is the resolution for this observation) was used for optical cross-matching. Since the positional accuracy of the catalogue is better than $1''$ (Mazumder et al. 2020), a nearest neighbour search algorithm was used to cross-match sources with the optical catalogue with a search radius r_s . The rate of contamination expected due to

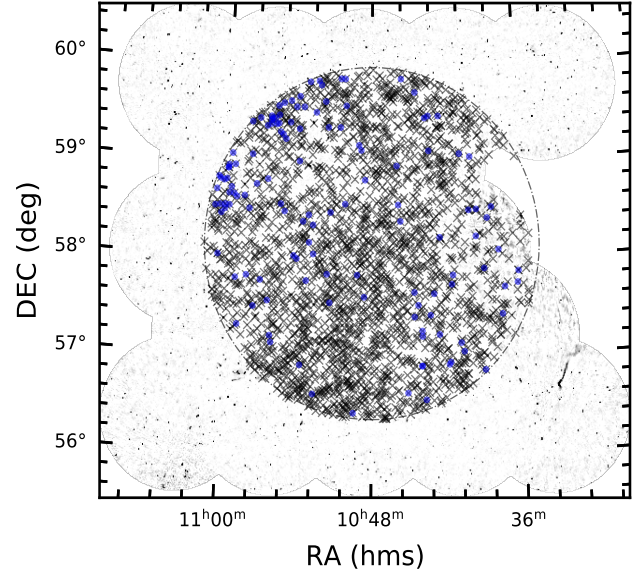


Figure 3. Sources with optical cross matches within 1.8° radius of phase center for the full mosaic. The area considered is represented by the black dot-dashed circle, and the sources in this region are represented by “x” marks. The blue circles represent the sources without any redshift matches.

proximity to optical sources is given by (Lindsay et al. 2014):

$$P_c = \pi r_s^2 \sigma_{opt}$$

where σ_{opt} is the surface density of the optical catalogue. For surface density of $1.4 \times 10^4 \text{ deg}^{-2}$, a matching radius $r_s = 9''$ gives a contamination of $<10\%$. This radius was thus used to ensure valid optical identification of a large number of radio sources.

Large FoVs are helpful for observational studies of like the one used here is useful for studying LSS, since the presence of a large number of sources provides statistically robust results and also reduces the effect of cosmic variance. Accordingly, the data used for this work had an FoV of $6^\circ \times 6^\circ$. However, cross-matching with optical catalogue produced matches with only 70% total sources over entire FoV, and 30% sources remained unclassified. Further investigation also revealed the presence of unknown systematics, which resulted in excess correlation and deviation from power-law behavior at large angles. The most probable cause for such a deviation seems to be either the presence of many sources with no redshifts at the field edge or the presence of artifacts at large distances from the phase center. Analysis done by reducing the area of the field increased percentage of optical matches and reduced the observed deviation from the power-law nature. Thus, the cause of such a deviation has been attributed to the former one.

Hence, the clustering properties of sources at large angular scales are not reliable for this observation. Thus, the analysis was restricted to a smaller area of the Lockman Hole region around the phase center; large-scale clustering properties could not be estimated. Taking a cut-off with 1.8° radius around the phase center resulted in $\sim 95\%$ sources having an optical counter-part. Hence, it is expected that the unclassified sources present would not affect the signal significantly (a detailed discussion on the choice of the FoV cut-off is discussed in Section 5). This FoV cut-off yielded 2555 sources in the radio catalogue, out of which 2424 sources have optical matches within the aforementioned match radius. This is shown in Figure 3, where the area considered is represented with black

dot-dashed circle, and the "x" marks denote the sources in radio catalogue; the blue circles represent the sources without any optical cross-matches in either photometry or spectroscopy. A total of 2415 photometric and 664 spectroscopic matches were obtained after the cross-match with optical catalogues. Out of these, 650 sources had both photometric and spectroscopic detection. For such cases, the spectroscopic identifications were taken. Combined photometry and spectroscopic identifications were obtained for a total of 2424 sources, of which 27 sources were discarded from this analysis since they were nearby objects with 0 or negative redshifts (Lindsay et al. 2014). The final sample thus had 2397 sources, which is $\sim 94\%$ of the total catalogued radio sources within 1.8° radius of the phase center. The redshift matching information for both the full and restricted catalogues have been summarised in Table 1. The redshift information from the optical catalogues was incorporated for these sources and was used for further analysis. Figure 4 shows the distribution of redshifts for the sources detected in both HELP and SDSS. In the left panel, the photometric redshifts are plotted as a function of the spectroscopic redshifts. As can be seen, the two values are in reasonable agreement with each other for most cases. Additionally to check for the reliability of obtained photometric redshifts, following Duncan et al. (2018), the outlier fraction defined by $\frac{|z_{\text{phot}} - z_{\text{spec}}|}{1 + z_{\text{spec}}} > 0.2$, is plotted as a function of the spectroscopic value (right panel of Figure 4). For this work, the drastic outliers are the points with values > 0.5 . The fraction of outliers with drastically different values between photometric and spectroscopic redshifts is $\sim 10\%$. While a detailed investigation is beyond the scope of this work, the outliers may be present due to the combination of uncertainties in the different surveys used in the HELP catalogue. As can be seen, the outlier fraction is not very drastic except for some cases; however, the reason for deviations in these sources is unknown. The median redshift for all the sources with redshift information comes out to be 0.78. The top panel of Figure 5 shows the distribution $N(z)$ as a function of source redshift, with the black dashed line indicating median redshift.

2.3 Classification using Radio Luminosity Function

The catalogued sources with optical counterparts were divided into AGNs and SFGs using their respective radio luminosities. Assuming pure luminosity evolution, the luminosity function evolves approximately as $(1+z)^{2.5}$ and $(1+z)^{1.2}$ for SFGs and AGNs respectively (McAlpine et al. 2013). The value for AGNs differ slightly from those of Smolčić et al. (2017) and Ocran et al. (2020) for the COSMOS field at 3 GHz and ELAIS N1 field at 610 MHz respectively. However, they are consistent with those of Prescott et al. (2016) for the GAMA fields. The values for redshift evolution of SFGs also agree broadly for the GAMA fields (Prescott et al. 2016) and the ELAIS N1 field (Ocran et al. 2019).

It has been shown in Magliocchetti et al. (2014, 2015, 2017) that radio selected galaxies powered by AGNs dominate for radio powers beyond a radio power $P_{\text{cross}}(z)$ which is related with the redshift z as:

$$\log_{10} P_{\text{cross}} = \log_{10} P_{0,\text{cross}} + z \quad (1)$$

upto $z \sim 1.8$, with P (at 1.4 GHz) in $\text{W Hz}^{-1} \text{sr}^{-1}$. In the local Universe, the value of P_{cross} is $10^{21.7} (\text{W Hz}^{-1} \text{sr}^{-1})$, coinciding with the observed break in the radio luminosity functions of SFGs (Magliocchetti et al. 2002), beyond which their luminosity functions decrease rapidly and the numbers are also reduced greatly. Thus contamination possibility between the two population of ra-

dio sources is very low using the radio luminosity based selection criterion (Magliocchetti et al. 2014, 2017).

The radio luminosity has been calculated for the sources from their flux as (Magliocchetti et al. 2014):

$$P_{1.4\text{GHz}} = 4\pi S_{1.4\text{GHz}} D^2 (1+z)^{3+\alpha} \quad (2)$$

where D is the angular diameter distance, and α is the spectral index of the sources in the catalogue. The individual spectral index for the sources was not used (since all sources do not have the measured values). The median value of 0.8 for α was derived by matching with high-frequency catalogues in Mazumder et al. (2020). Since the probability of finding a large number of bright, flat-spectrum sources is very low (Magliocchetti et al. 2017), the median value of 0.8 was used to determine the luminosity functions of the sources in the Lockman Hole field detected here.

Besides the radio luminosity criterion described above, there are several other methods to classify sources into AGNs and SFGs. X-ray luminosity can also be used to identify AGNs since it can directly probe their high energy emissions (Szokoly et al. 2004). Color-color diagnostics from optical data (like IRAC) can also be used for identifying AGNs (Donley et al. 2012). Classification can also be done using the q_{24} parameter, which is the ratio of 24 μm flux density to the effective 1.4 GHz flux density (Bonzini et al. 2013). Based on the results of McAlpine et al. (2013), it was shown by Magliocchetti et al. (2014) that the radio luminosity function for SFGs fall of in a much steeper manner than AGNs for all redshifts, and this reduces the chances of contamination in the two samples. Additionally, these different multi-wavelength methods are not always consistent with each other, and a detailed investigation into any such discrepancy is beyond the scope of this work. Hence, only the radio luminosity criterion has been used for classification.

The sources with redshifts up to 1.8 were classified into AGNs and SFGs according to whether their luminosity is greater than or less than the threshold in Equation 1 (with P_{cross} determined using Equation 2). At higher redshifts (i.e. > 1.8), $P_{0,\text{cross}}$ is fixed to $10^{23.5} [\text{W Hz}^{-1} \text{sr}^{-1}]$ (McAlpine et al. 2013). Of the 2397 sources, 1821 were classified as AGNs and 576 as SFGs using the radio luminosity criteria. The median redshifts for AGNs and SFGs are 1.02 and 0.2 respectively.

3 ESTIMATION OF CORRELATION FUNCTION: COMBINED SOURCES

3.1 The Angular Correlation Function

The angular two-point correlation function $w(\theta)$ is used to quantify clustering in the sky on angular scales. While several estimators have been proposed in literature (for a comparison of the different types of estimators see Kerscher et al. (2000) and Appendix B. of Siewert et al. (2020)), this work uses the LS estimator proposed by Landy & Szalay (1993). It is defined as :

$$w(\theta) = \frac{DD(\theta) - 2DR(\theta) + RR(\theta)}{RR(\theta)} \quad (3)$$

Here $DD(\theta)$ and $RR(\theta)$ are the normalised average pair count for objects at separation θ in the original and random catalogues, respectively. Catalogue realizations generated by randomly distributing sources in the same field of view as the real observations have been used to calculate $RR(\theta)$. The LS estimator also includes the normalized cross-pair separation counts $DR(\theta)$ between original and random catalogue, which has the advantage of effectively reducing the large-scale uncertainty in the source density (Landy &

Table 1. Summary of number of sources with redshift information

Area	Number of sources	Redshift matches	Percentage of matches	AGNs	SFGs
$6^\circ \times 6^\circ$	5489	3628	66	2149	1479
3.6° diameter around phase center	2555	2397	95	1821	576

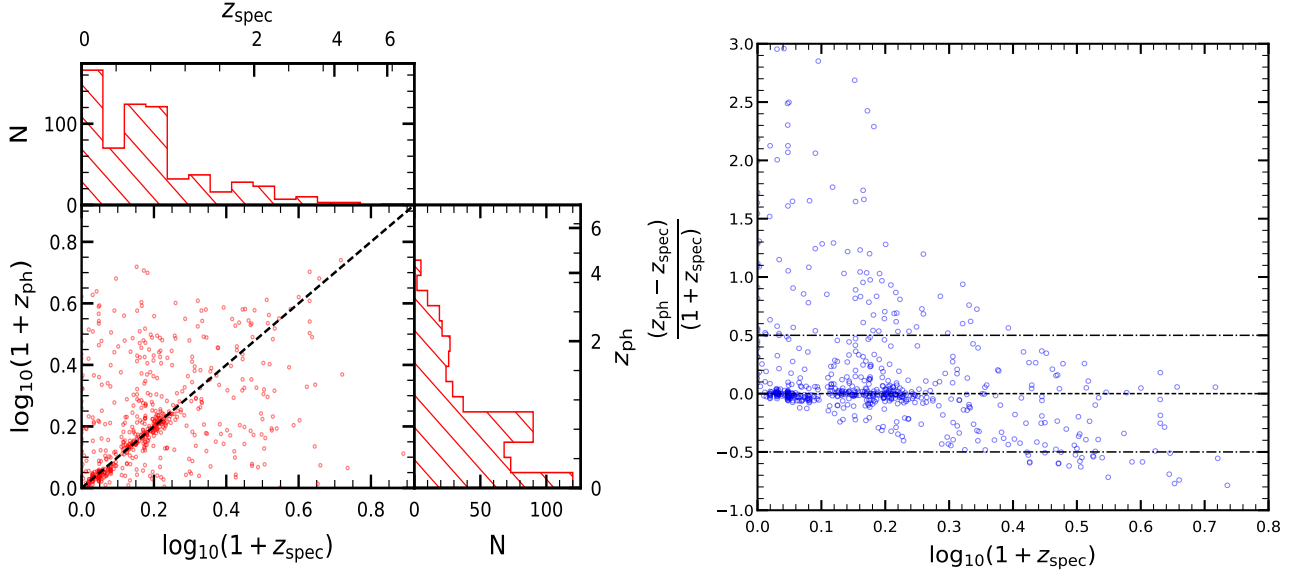


Figure 4. Comparison of photometric and spectroscopic redshifts for the sources with matches for both. **(left panel)** Photometric redshift plotted as a function of the spectroscopic redshift, with the black dashed line indicating equal values for both. The redshift distribution is shown via the histograms for photometric (right subplot) and spectroscopic (top subplot). **(right panel)** Distribution of $\frac{z_{\text{ph}} - z_{\text{spec}}}{1 + z_{\text{spec}}}$ plotted as a function of z_{spec} . The black dashed line represents 0 deviation between the photometric and spectroscopic redshifts.

Szalay 1993; Hamilton 1993; Blake & Wall 2002a; Overzier et al. 2003). The uncertainty in the determination of $w(\theta)$ is calculated using the bootstrap resampling method (Ling et al. 1986), where 100 bootstrap samples are generated to quote the 16th and 84th percentile errors in determination of $w(\theta)$.

3.1.1 Random Catalogue

The random catalogues generated should be such that any bias due to noise does not affect the obtained values of the correlation function. The noise across the entire $6^\circ \times 6^\circ$ mosaic of the field is not uniform (see Figure 3 of Mazumder et al. (2020)). This can introduce a bias in estimating the angular two-point correlation function since the non-uniform noise leads to the non-detection of fainter sources in the regions with higher noise.

PvBDSF was used for obtaining the noise map of the image. Assuming the sources follow a flux distribution of the form $dN/dS \propto S^{-1.6}$ (Intema et al. 2011; Williams et al. 2013), random samples of 3000 sources were generated in the given flux range (with lower limit corresponding to 2 times the background RMS of the image) and assigned random positions to distribute them in the entire FoV. The sources constitute a mixture of 70% unresolved sources and 30% extended sources, which is roughly in the same ratio as the actual source catalogue (Mazumder et al. 2020). These were injected into the residual map, and using the same parameters in PvBDSF as the ones used in the extraction of the original sources (see Mazumder et al. (2020)), the random catalogues were extracted.

100 such statistically independent realizations were used to reduce the associated statistical uncertainty.

For clustering analysis of AGNs and SFGs, two sets of random catalogues were generated using the publicly available catalogues for these source types from the T-RECS simulation (Bonaldi et al. 2018). These catalogues have source flux densities provided at different frequencies between 150 MHz to 20 GHz. The flux densities at 300 MHz were considered for the randoms. They were scaled to 325 MHz using $\alpha = 0.8$, and 2000 sources were randomly chosen within flux density limit for the radio catalogue of AGNs and SFGs. They were assigned random positions within the RA, Dec limits of the original catalogues and injected into the residual maps. Then using the same parameters for PvBDSF as the original catalogue, the sources were recovered. 100 such realizations were done for AGNs and SFGs separately. The recovered random catalogues were used for further clustering analysis of the classified populations. It should also be mentioned here that the lower cut-off of flux density for the random catalogues was ~ 0.1 mJy, which is 2 times the background RMS. As already seen from Mazumder et al. (2020), even a flux limit of 0.2 mJy (4 times the background RMS) takes care of effects like the Eddington bias (Eddington 1913). Thus 0.1 mJy is taken as the limiting flux for both the combined and the the classified random catalogues. The final random samples for AGNs and SFGs consisted of a total of ~ 120000 sources each, while for the combined sample, it was ~ 200000 . This is much higher than the number of sources in the radio catalogue. Thus, it does not dominate the errors. As has already been stated, the point and extended

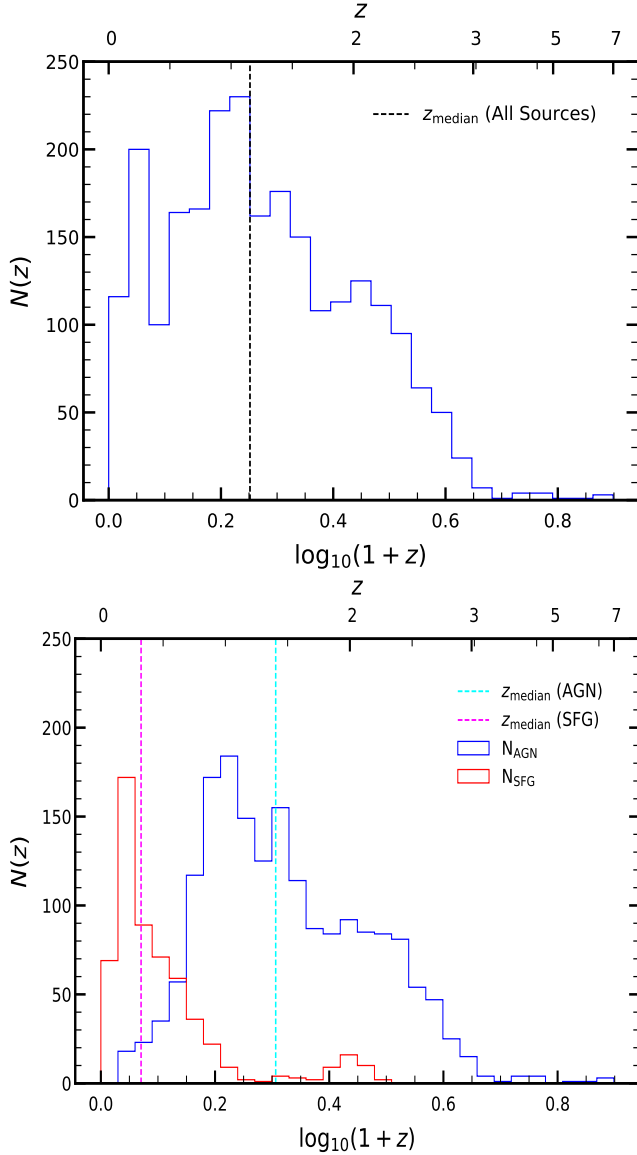


Figure 5. Redshift distribution ($N(z)$) for sources with either photometric (HELP) or spectroscopic (SDSS) redshifts. The top panel shows $N(z)$ distribution for all sources with the black dashed line indicating the median redshift for all sources. The bottom shows the same for sources classified into AGNs (blue curve) and SFGs (red curve) using the radio luminosity criterion discussed in the text, with the cyan and magenta dashed lines indicating the respective median redshifts.

sources in the random catalogues (generated for the whole sample and the classified sources) are taken in the same ratio as that of the original radio catalogue. The drawback of this assumption is that there is a chance of underestimating extended sources in the random catalogue, which may lead to spurious clustering signals at smaller angular scales. However, since no evidence of any spurious signal is seen, taking point and extended sources in the same ratio as the original catalogue seem reasonable.

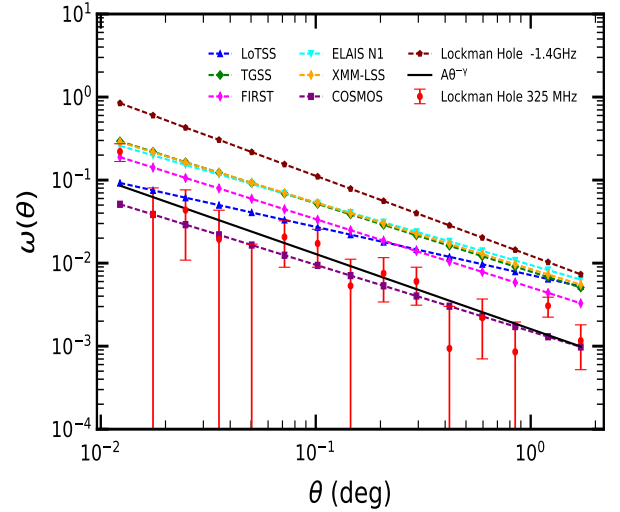


Figure 6. Angular correlation function for all sources in the Lockman Hole region at 325 MHz. The dashed black line is the best-fitting power law to $w(\theta)$. Comparison has been done with best fitted power laws obtained from previous studies of LoTSS (blue triangle, Siewert et al. 2020), TGSS-ADR (green diamonds, Rana & Bagla 2019), FIRST (magenta thin diamonds, Lindsay et al. 2014), ELAIS-N1 (cyan inverted triangles, Chakraborty et al. 2020), XMM-LSS (orange thin diamonds, Hale et al. 2019), COSMOS (purple squares, Hale et al. 2018), & Lockman Hole 1.4 GHz observation (maroon pentagons, Bonato et al. 2020). Different studies mentioned here have different flux density limits (see Table 2).

3.2 Angular Clustering Pattern at 325 MHz

The angular correlation function of the sources detected in this observation is calculated using the publicly available code *TreeCorr*⁸ (Jarvis et al. 2004). The 325 MHz catalogue was divided into 15 equispaced logarithmic bins between $\theta \sim 36''$ to 2° . The lower limit corresponds to the four times the PSF at 325 MHz, and the upper limit is the half-power beamwidth at this frequency. Figure 6 shows the angular correlation function of the 325 MHz in red circles; the error bars are estimated using the bootstrap method as discussed earlier. A power law of the form $w(\theta) = A\theta^{1-\gamma}$ is also fitted. The power law index, γ is kept fixed at the theoretical value of 1.8. The parameter estimation for this fit is done using Markov chain Monte Carlo (MCMC) simulation by generating 10^6 data points by applying the Metropolis-Hastings algorithm in the A parameter space. The first 10^2 samples have been removed from the generated chains to avoid the burn-in phase. From the sampled parameter space, χ^2 is used to estimate the most likely values of the parameters. The best fit parameters are $\log(A) = -2.73^{+0.11}_{-0.15}$, with the error bars being the $1-\sigma$ error bars from the 16th and 84th percentiles of the chain points.

3.2.1 Comparison with previous Observations

The best fit values obtained for parameters A and γ of the 325 MHz catalogue have been compared with those for other observations at radio frequencies. The parameters obtained for different radio

⁸ <https://github.com/rmjarvis/TreeCorr>

surveys, namely from Lindsay et al. (2014); Hale et al. (2018, 2019); Rana & Bagla (2019); Chakraborty et al. (2020); Bonato et al. (2020); Siewert et al. (2020) have been summarised in Table 2. The best-fit estimate of the slope γ for the correlation function is found to be in reasonable agreement with the theoretical prediction of Peebles (1980) and previous observations (for example see Bonato et al. (2020); Siewert et al. (2020)). The scaled flux limit at 325 MHz for the Bonato et al. (2020) catalogue at (originally 1.4 GHz, scaled using a spectral index of 0.8) is ~ 0.4 mJy, very close to the flux limit for this work. However, their estimates are higher than all previous estimates (they particularly compare with (Magliocchetti et al. 2017)), which they assign partly to the presence of sample variance. While the area probed by (Bonato et al. 2020) is also included within the region this work probes, the area covered are different, the one covered here being larger. This might be the reason for differences between the estimates in this work and (Bonato et al. 2020), despite both having similar flux density cut-offs. The clustering amplitude for this work is similar to Hale et al. (2018) at almost all the angular scales. One possible reason is that the flux limit for the study at 3 GHz was 5.5 times the $2.3 \mu\text{Jy beam}^{-1}$ limit corresponding to a flux of ~ 0.1 mJy at 325 MHz, which is near the flux cut-off for this work (0.3 mJy), and thus can trace similar halo masses and hence clustering amplitudes.

The clustering properties of the radio sources in the VLA-FIRST survey (Becker et al. 1995) has been reported in Lindsay et al. (2014), where $\log(A)$ is $-2.30^{+0.70}_{-0.90}$. Hale et al. (2018) and Hale et al. (2019) have reported $\log(A)$ value of -2.83 and -2.08 for the COSMOS and XMM-LSS fields, respectively, by fixing γ at the theoretical value of 1.80. The clustering amplitude of the 150 MHz TGSS-ADR (Intema et al. 2017) has been shown by Rana & Bagla (2019) for a large fraction of the sky and at different flux density cut-offs. In the recent deep surveys of the ELAIS-N1 field at 400 MHz (Chakraborty et al. 2020), $\log(A)$ and the best fit power law index have the values $-2.03^{+0.10}_{-0.08}$ and 1.75 ± 0.06 respectively.

Comparison has also been made with the wide-area survey of LoTSS data release 1 (Siewert et al. 2020). This study (with data obtained at a central frequency of 144 MHz) employed various masks on the data to obtain the angular clustering values. The survey covers a wider area, but the flux cut-off threshold is above 1 mJy for all of the masks due to systematic uncertainties. A wide range of angles, $0.1^\circ \leq \theta \leq 32^\circ$ was fixed to determine the angular clustering. Taking three different flux density limits- at 1, 2 and 4 mJy and different masks, the values of $\log(A)$ and power-law index were obtained (the fitting for the power-law form was done for $0.2^\circ \leq \theta \leq 2^\circ$). Siewert et al. (2020) have applied various flux density cuts and masks to their sample for obtaining the angular clustering parameters. They have concluded that the flux density cut-off of 2 mJy provides the best estimate for the angular clustering parameters, and the same has been used here for comparison. Comparison of the present work with LoTSS 2 mJy flux cut shows that the values of $\log(A)$ agree well. The best fit power-law index is also consistent within 1σ error bars. Hence, it is seen that the angular correlation function obtained in the present work gives values for the parameters $\log(A)$ and γ consistent with those reported in previous surveys. Additionally, since this survey has both wider coverage than the recent EN1 data and a lower flux density threshold than the LoTSS data used by Siewert et al. (2020), it provides an intermediate data set along a different line of sight to probe cosmology.

3.3 The Spatial Correlation Function at 325 MHz

For known angular clustering $w(\theta)$, the spatial clustering of sources is quantified by the two-point correlation function $\xi(r)$. Using the Limber inversion (Limber 1953), $\xi(r)$ can be estimated for known redshift distribution. Gravitational clustering causes the spatial clustering to vary with redshift, and thus a redshift dependent power-law spatial correlation function can be defined as (Limber 1953; Overzier et al. 2003):

$$\xi(r, z) = (r_0/r)^\gamma (1+z)^{\gamma-(3+\epsilon)} \quad (4)$$

where the clustering length r is in comoving units, ϵ specifies clustering models (Overzier et al. 2003) and r_0 is the clustering length at $z=0$. For this work, comoving clustering model, in which the correlation function is unchanged in the comoving coordinate system and with $\epsilon = \gamma-3$, is used. The comoving cluster size is constant. The correlation length is calculated using (Peebles 1980):

$$A = r_0^\gamma H_\gamma (H_0/c) \frac{\int_0^\infty N^2(z) (1+z)^{\gamma-(3+\epsilon)} \chi^{1-\gamma}(z) E(z) dz}{[\int_0^\infty N(z) dz]^2} \quad (5)$$

$$\text{where } H_\gamma = \frac{\Gamma(\frac{1}{2})\Gamma(\frac{\gamma-1}{2})}{\Gamma(\frac{\gamma}{2})},$$

$E(z) = \sqrt{\Omega_{m,0}(1+z)^3 + \Omega_{k,0}(1+z)^2 + \Omega_{\Lambda,0}}$ is the cosmological factor, $N(z)$ is the redshift distribution of the sources and $\chi(z)$ is the line of sight comoving distance. Equation 5 can be used to estimate r_0 using the angular clustering amplitude A and the redshift distribution shown in Figure 5.

The theoretical value of 1.8 for γ , as predicted by Peebles (1980) is consistent with the values across various surveys, as well as within 2σ of the current analysis (tabulated in Table 2). Thus the theoretical value of γ , the distribution of A obtained from the MCMC distribution discussed in 3.2 and the combined redshift distribution discussed in Section 2.2 are used to estimate the value of r_0 . Figure 7 shows the probability distribution function (PDF) of the spatial clustering length. As already mentioned, the median redshift of the samples is ~ 0.78 , and at this redshift, the median value of r_0 is $3.50^{+0.50}_{-0.50} \text{ Mpc h}^{-1}$, where the errors are the 16th and 84th percentile errors.

3.4 The Bias Parameter

The bias parameter is used to quantify the relation between the clustering property of luminous sources and the underlying dark matter distribution. The ratio of the galaxy to the dark matter spatial correlation function is known as the scale-independent linear bias parameter $b(z)$ (Kaiser 1984; Bardeen et al. 1986; Peacock & Smith 2000). For cosmological model with dark matter governed only by gravity, following Lindsay et al. (2014); Hale et al. (2018); Chakraborty et al. (2020), $b(z)$ is calculated as :

$$b(z) = \left(\frac{r_0(z)}{8} \right)^{\gamma/2} \frac{J_2^{1/2}}{\sigma_8 D(z)/D(0)} \quad (6)$$

where $J_2 = 72/[(3-\gamma)(4-\gamma)(6-\gamma)2^\gamma]$, $D(z)$ is the linear growth factor, calculated from CMB and galaxy redshift information (Eisenstein et al. 1999), and σ_8^2 is the amplitude of the linear power spectrum on a comoving scale of 8 Mpc h^{-1} .

For this work, the bias parameter has been calculated using the median redshift value of the r_0 distribution with the 16th and 84th percentile errors. The value of the bias parameter $b(z)$ at $z=0.78$ is $2.22^{+0.33}_{-0.36}$.

Table 2. Clustering Parameters for Observed Data. The columns indicate the name of the survey (Observation), observing frequency in MHz (Frequency), the flux density cut-off at the observing frequency ($S_{\text{cut},\nu}$), the equivalent 325 MHz flux-density ($S_{\text{cut},325}$), best fit clustering amplitude ($\log_{10}(A)$) and best fit power-law index (γ) respectively.

Observation	Frequency (MHz)	$S_{\text{cut},\nu}^{\dagger}$ (mJy)	$S_{\text{cut},325}^*$	$\log_{10}(A)$	γ	Reference
FIRST	1400	1.00	3.21	$-2.30^{+0.70}_{-0.90}$	$1.82 \pm .02$	Lindsay et al. (2014)
COSMOS	3000	0.013	0.08	$-2.83^{+0.10}_{-0.10}$	1.80	Hale et al. (2018)
XMM-LSS	144	1.40	0.73	$-2.08^{+0.05}_{-0.04}$	1.80	Hale et al. (2019)
TGSS-ADR	150	50	26.9	$-2.11^{+0.30}_{-0.30}$	$1.82 \pm .07$	Rana & Bagla (2019)
ELAIS-N1	400	0.10	0.12	$-2.03^{+0.10}_{-0.08}$	1.75 ± 0.06	Chakraborty et al. (2020)
Lockman Hole	1400	0.12	0.39	$-1.95^{+0.005}_{-0.005}$	$1.96 \pm .15$	Bonato et al. (2020)
LoTSS	144	2.00	1.04	$-2.29^{+0.6}_{-0.6}$	$1.74 \pm .16$	Siewert et al. (2020)
Lockman Hole	325	0.30	0.30	$-2.73^{+0.11}_{-0.15}$	1.80	This work

$^{\dagger} S_{\text{cut},\nu}$ is the flux density limit at the respective observing frequencies; $^* S_{\text{cut},325}$ is the scaled flux density ($\alpha=0.8$) limit at 325 MHz

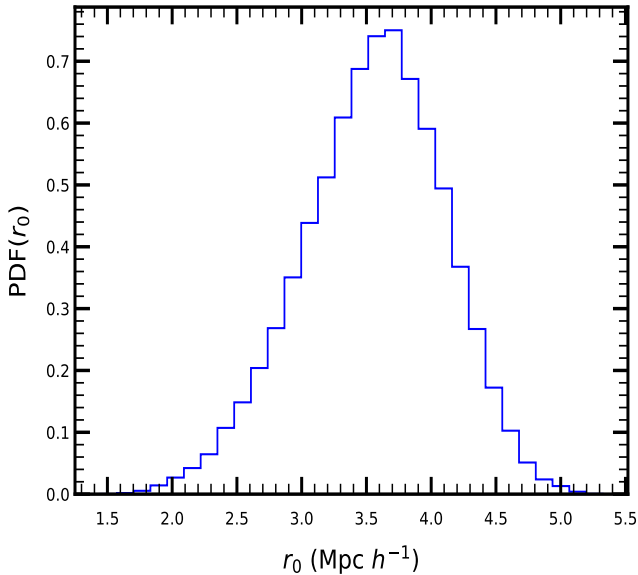


Figure 7. Probability distribution function of spatial clustering length (r_0) for the entire sample at 325 MHz.

4 ESTIMATION OF CORRELATION FUNCTION: AGNS AND SFGS

This section discusses the angular and spatial correlation scales and the bias parameter obtained for the two separate populations of sources (i.e., AGNs and SFGs). The obtained values are also compared with previously reported values using radio and other bands data. Following a similar procedure as that done for the entire population, initially, the angular clustering was calculated, and a power law of the form $A\theta^{1-\gamma}$ was fitted. The best value of clustering amplitude A is determined, once again keeping γ fixed at the theoretical value of 1.8 for both AGNs and SFGs populations. Figure 8 shows the angular correlation function of AGNs (left panel) and SFGs(right panel). Using the MCMC simulations as discussed previously, the clustering amplitudes, $\log(A)$ have values $-2.18^{+0.20}_{-0.20}$ and $-1.69^{+0.10}_{-0.10}$ respectively for AGNs and SFGs. The results of the fit and the subsequent values of clustering length and bias pa-

rameter obtained here and results from previous surveys in radio wavelengths are also tabulated in Table 3.

The spatial clustering length and bias parameter b_z for the AGNs with $z_{\text{median}}=1.02$ are $8.30^{+0.96}_{-0.91}$ Mpc h^{-1} and $3.74^{+0.39}_{-0.36}$. For SFGs with $z_{\text{median}} \approx 0.20$, the values are $r_0 = 3.22^{+0.34}_{-0.32}$ Mpc h^{-1} and $b_z = 1.06^{+0.1}_{-0.1}$. It is seen that the spatial clustering length and consequently the bias factor for AGNs is more than SFGs, which implies that the latter are hosted by less massive haloes, in agreement with previous observations (Gilli et al. 2009, 2007; Starikova et al. 2012; Dolley et al. 2014; Magliocchetti et al. 2017; Hale et al. 2018; Chakraborty et al. 2020).

4.1 Comparison with previous Observations

Figure 9 shows the observationally determined values from surveys at various wavebands for r_0 as a function of their redshift, while Figure 10 shows the same for the bias parameter. The left and right panels of Figure 9 are for AGNs and SFGs, respectively. Table 3 summarizes the values obtained in radio surveys only, while Figures 9, 10 show the observed values for surveys at radio as well as other wavebands, e.g. IR and X-Ray.

The clustering length for AGNs in this work is at $z_{\text{median}} \approx 1.02$ is $8.30^{+0.96}_{-0.91}$ Mpc h^{-1} . Using X-Ray selected AGNs in the COSMOS field, Gilli et al. 2009 obtained clustering lengths at redshifts upto ~ 3.0 . They divided their sample into a number of bins, to obtain r_0 at different median redshifts. For their entire sample, taking slope of the angular correlation function as 1.80, r_0 was $8.39^{+0.41}_{-0.39}$ Mpc h^{-1} , for a median redshift of 0.98. It is consistent with the value obtained here at a similar redshift. The clustering length with this work is also consistent within error bars for AGNs at 400 MHz and 610 MHz of Chakraborty et al. (2020). For their work, they obtain an r_0 value of $7.30^{+1.14}_{-1.12}$ Mpc h^{-1} at $z \approx 0.91$, $6.00^{+1.5}_{-1.3}$ Mpc h^{-1} at $z_{\text{median}} = 0.84$. The clustering length estimates for radio selected AGNs in the COSMOS field at 1.4 GHz (Magliocchetti et al. 2017) and 3 GHz (Hale et al. 2018) observed with the VLA also agree within error bars with the estimates obtained here. Magliocchetti et al. (2017) have found a clustering length of $7.84^{+1.75}_{-2.31}$ Mpc h^{-1} at $z \approx 1.25$ while (Hale et al. 2018) obtained $6.90^{+0.60}_{-0.70}$ Mpc h^{-1} , $9.60^{+0.70}_{-0.70}$ Mpc h^{-1} and $7.30^{+0.90}_{-0.90}$ Mpc h^{-1} at $z \approx 0.70, 1.24, 1.77$ respectively. Using X-ray selected AGNs in the CDFS field, Gilli et al. (2005) obtained a value of $10.30^{+1.7}_{-1.7}$ Mpc

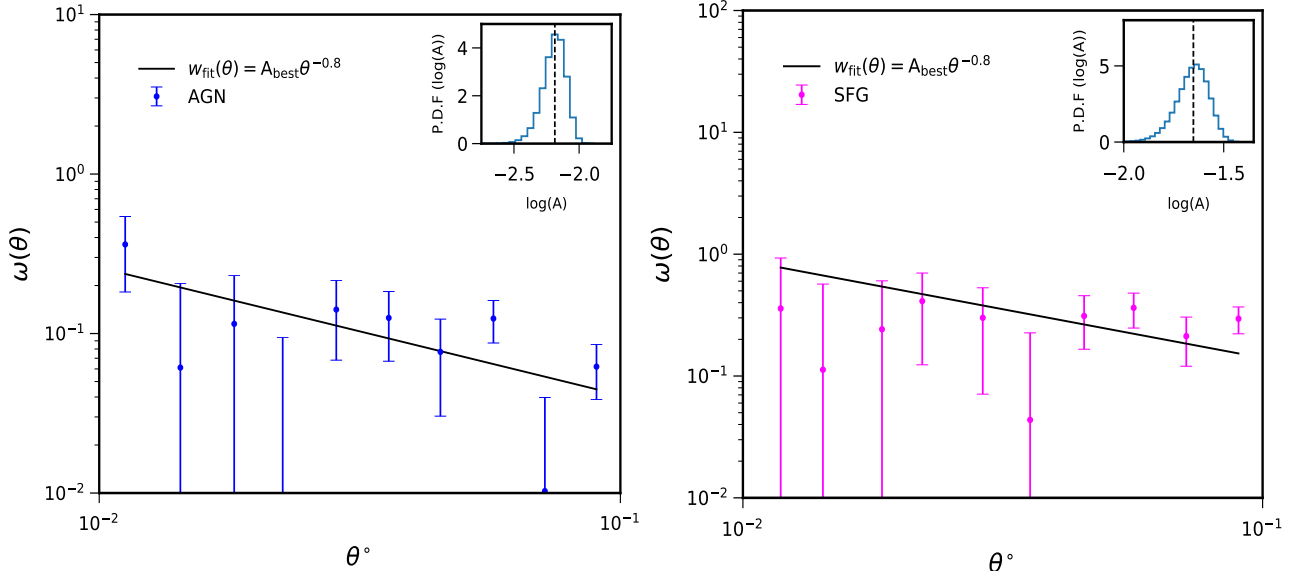


Figure 8. Angular correlation function for sources classified as AGNs (left panel) and SFGs (right panel). The slope of the best fit function γ is fixed at 1.8 and the distribution of correlation amplitude (A) is shown in the inset of each panel.

Table 3. Spatial Clustering Length and Bias Parameter from Different Observations. The columns are respectively name of the survey field, observing frequency in MHz, type of radio source (AGNs/SFGs), median redshift, angular clustering amplitude, spatial clustering length in Mpc h^{-1} & bias parameter value.

Observation	Frequency (MHz)	Source type	z_{median}	$\log_{10}(A)$	r_0 (Mpc h^{-1})	$b_{z_{\text{median}}}$	Reference
COSMOS	3000	AGNs	0.70	$-2.30^{+0.1}_{-0.1}$	$6.9^{+0.60}_{-0.70}$	$2.1^{+0.2}_{-0.2}$	Hale et al. (2018)
		AGNs	1.24	$-2.60^{+0.1}_{-0.1}$	$9.6^{+0.70}_{-0.70}$	$3.6^{+0.2}_{-0.2}$	
		AGNs	1.77	$-2.60^{+0.1}_{-0.1}$	$7.3^{+0.30}_{-0.90}$	$3.5^{+0.2}_{-0.4}$	
		SFG	0.62	$-2.60^{+0.1}_{-0.1}$	$5.0^{+0.50}_{-0.60}$	$1.5^{+0.1}_{-0.2}$	
		SFG	1.07	$-2.90^{+0.1}_{-0.1}$	$6.1^{+0.60}_{-0.70}$	$2.3^{+0.2}_{-0.2}$	
VLA-COSMOS	1400	AGNs	1.25	$-2.79^{+0.1}_{-0.1}$	$7.84^{+1.75}_{-2.31}$	-	Magliocchetti et al. (2017)
		SFG	0.50	$-2.36^{+0.3}_{-0.3}$	$5.46^{+1.12}_{-2.10}$	-	
ELAIS N1	400	AGNs	0.91	$-2.22^{+0.16}_{-0.16}$	$7.30^{+1.4}_{-1.2}$	$3.17^{+0.5}_{-0.5}$	Chakraborty et al. (2020)
		SFG	0.64	$-2.16^{+0.05}_{-0.06}$	$4.62^{+0.39}_{-0.40}$	$1.65^{+0.14}_{-0.14}$	
ELAIS N1	612	AGNs	0.85	$-2.30^{+0.02}_{-0.03}$	$6.0^{+1.5}_{-1.3}$	$2.6^{+0.6}_{-0.5}$	Chakraborty et al. (2020)
		SFG	0.87	$-2.19^{+0.01}_{-0.02}$	$4.16^{+0.7}_{-0.8}$	$1.59^{+0.2}_{-0.2}$	
Lockman Hole	325	AGNs	1.02	$-2.18^{+0.20}_{-0.20}$	$8.30^{+0.96}_{-0.91}$	$3.74^{+0.39}_{-0.10}$	This work
		SFG	0.20	$-1.65^{+0.1}_{-0.1}$	$3.22^{+0.34}_{-0.32}$	$1.06^{+0.10}_{-0.10}$	

h^{-1} at $z \approx 0.84$. This value though higher than the values for radio selected AGNs, is still consistent within error bars.

For the SFGs population (right panel of Figure 9), the median redshift is 0.20. At this redshift, the clustering length is $3.22^{+0.34}_{-0.32} \text{ Mpc h}^{-1}$. This estimate is at a redshift lower than previous observations. An extensive study at mid-IR frequency has been done by Dolley et al. (2014) for SFGs. The lowest redshift probed in their study is 0.31, where r_0 is $3.41^{+0.18}_{-0.18} \text{ Mpc h}^{-1}$. Thus, the value is consistent with that obtained here at a nearby redshift. Magliocchetti et al. (2013) studied the clustering of SFGs using the Herschel PACS Evolutionary Probe observations of the COSMOS and Extended Groth Strip fields. They found clustering lengths for SFGs out to $z \approx 2$. For the ELAIS-N1 field at 400 MHz and 610 MHz,

Chakraborty et al. (2020) reported clustering length of $4.62^{+0.39}_{-0.40} \text{ Mpc h}^{-1}$ and $4.16^{+0.70}_{-0.80} \text{ Mpc h}^{-1}$ at redshifts 0.64 and 0.87 respectively. The 3 GHz COSMOS field studies of Hale et al. (2018) gave clustering lengths $5.00^{+0.50}_{-0.60} \text{ Mpc h}^{-1}$ and $6.1^{+0.60}_{-0.70} \text{ Mpc h}^{-1}$ respectively at $z \approx 0.62$ and 1.07. The mid-IR selected samples for Lockman Hole give r_0 values $4.98^{+0.28}_{-0.28} \text{ Mpc h}^{-1}$ and $8.04^{+0.69}_{-0.69} \text{ Mpc h}^{-1}$ at $z \approx 0.7$ and 1.7 respectively. Similarly, the mid-IR sample for Gilli et al. (2007) has clustering lengths r_0 is $4.25^{+0.12}_{-0.12} \text{ Mpc h}^{-1}$ and $3.81^{+0.10}_{-0.10} \text{ Mpc h}^{-1}$ for $z \approx 0.67$ and 0.73.

The results have also been compared with the assumed bias models of the semi-empirical simulated catalogue of the extragalactic sky, the Square Kilometer Array Design Studies (referred to as SKADS henceforth, Wilman et al. 2008). This simulation models

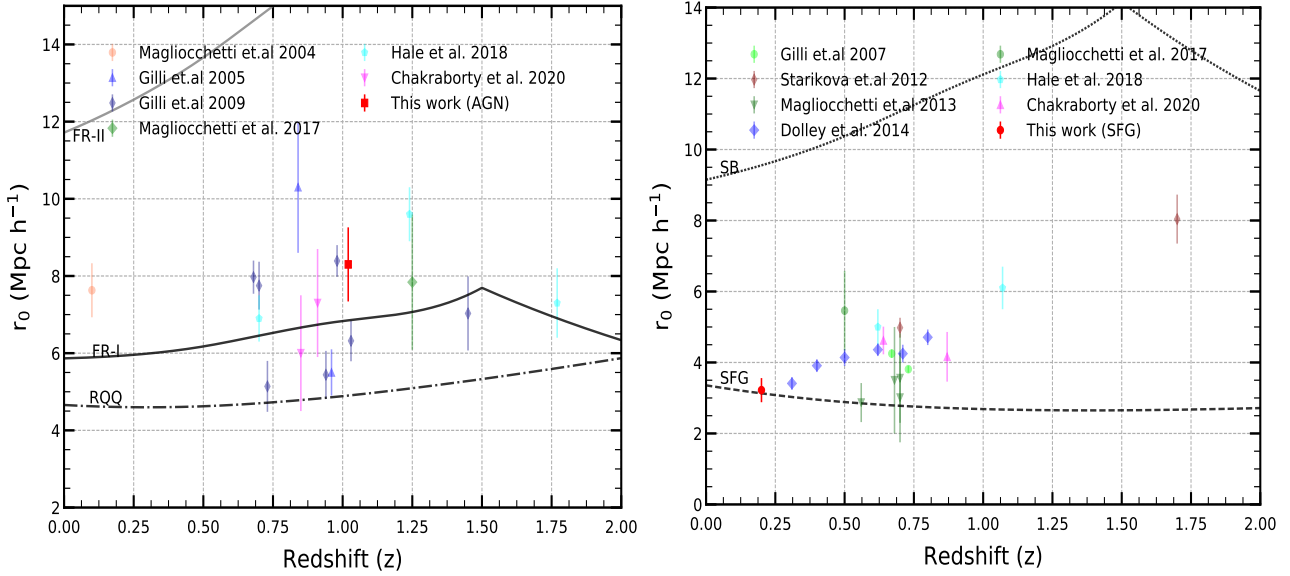


Figure 9. (left panel) Spatial correlation length (r_0) for AGNs as a function of redshift (red square). For comparison, the values for the same obtained by Magliocchetti et al. (2004) (orange circle), Gilli et al. (2005) (blue triangle), Gilli et al. (2009) (purple square), Magliocchetti et al. (2017) (green diamonds), Hale et al. (2018) (cyan circles) & Chakraborty et al. (2020) (magenta inverted triangle) have been plotted. Predictions from SKADS (Wilman et al. 2008) have also been plotted for Radio Quiet Quasars (RQQ), FR-I and FR-II radio galaxies. **(right panel)** Spatial correlation length (r_0) SFGs as a function of redshift (red circle). For comparison, values obtained by Gilli et al. (2007) (black circles), Starikova et al. (2012) (maroon diamonds), Magliocchetti et al. (2013) (green inverted triangles), Dolley et al. (2014) (blue diamonds), Magliocchetti et al. (2017) (green circles), Hale et al. (2018) (cyan pentagon), & Chakraborty et al. (2020) (magenta triangles) have been plotted. Predictions from SKADS (Wilman et al. 2008) have also been plotted for SFGs and Starburst galaxies (SB).

the large-scale cosmological distribution of radio sources to aid the design of next-generation radio interferometers. It covers a sky area of $20^\circ \times 20^\circ$, with sources out to a cosmological redshift of $z \sim 2.0$ and a minimum flux 10 nJy at 151, 610 MHz & 1.4, 4.86 and 18 GHz. The simulated sources are drawn from observed and, in some cases, extrapolated luminosity functions on an underlying dark matter density field with biases to reflect the measured large-scale clustering. It uses a numerical Press–Schechter (Press & Schechter 1974) style filtering on the density field to identify clusters of galaxies. The SKADS catalogue has been used here for statistical inference of the spatial and angular clustering variations of the sources with redshift. It should be mentioned here that the T-RECS catalogue (Bonaldi et al. 2018) incorporates more updated results from the recent observations. However, the evolution of the bias parameter and clustering length with redshift is not available for the same; hence SKADS has been used.

The bias parameter for AGNs and SFGs at $z_{\text{median}} 1.02$ and 0.20 is $3.74^{+0.39}_{-0.36}$ and $1.06^{+0.10}_{-0.10}$ respectively. Although the value for AGNs is slightly higher than those obtained by Hale et al. (2018) and Chakraborty et al. (2020), it is still with reasonable agreement with the SKADS for FR-I galaxies. Comparison with the population distribution of the SKADS simulation of Wilman et al. (2008), in terms of both clustering length and the bias parameter (solid magenta pentagons in Figure 10) show that the AGN population is dominated by FR-I type galaxies hosted in massive haloes with $\sim M_h = 5 \times 10^{13} h^{-1} M_\odot$. It can also be seen from Figure 10, that the mass of the haloes hosting the SFG samples of the current sample is $\sim M_h = 3 \times 10^{12} h^{-1} M_\odot$. Thus, it is seen that the SFGs have a lower range of halo masses compared to AGNs, which implies that the latter inhabits more massive haloes and are more biased tracers of the dark matter density field.

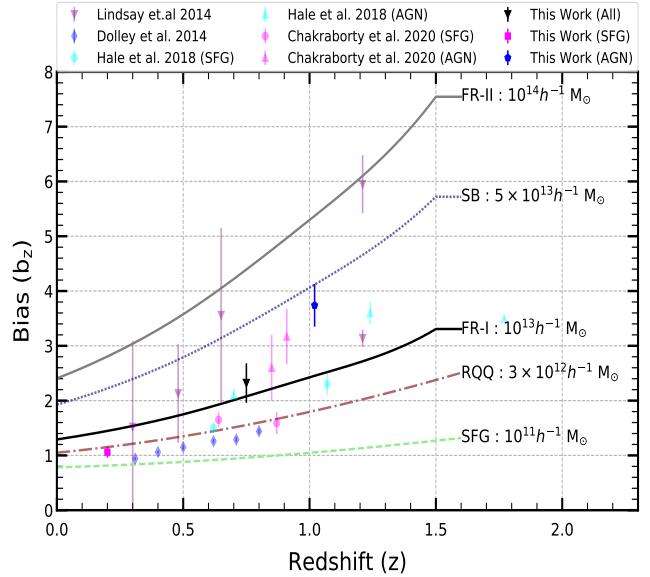


Figure 10. Bias parameter b_z for whole population (black inverted triangle) as well AGNs (blue pentagons) and SFGs (magenta squares). Bias parameters from previous observations by Lindsay et al. (2014) (purple inverted triangles), Dolley et al. (2014) (blue diamonds), Hale et al. (2018) (cyan triangles for AGNs and cyan circles SFGs) & Chakraborty et al. (2020) (magenta triangles and circles for AGNs and SFGs respectively) are shown. Predictions from SKADS is also shown by the continuous curves.

5 DISCUSSION

The analysis of clustering properties of radio selected sources in the Lockman Hole region presented in this work is one of the first results

reported at 325 MHz. Similar studies were previously done at 400 MHz for the ELAIS-N1 field (Chakraborty et al. 2020), however for a much smaller area. Beside analysing at a mostly unexplored frequency, this work also presents a comparatively large area with a significant number of sources. Previous clustering study of the same area using 1.4 GHz data from WSRT by Bonato et al. (2020) used 1173 sources with a flux density cut-off of 0.12 mJy at 1.4 GHz (or 0.4 mJy at 325 MHz). Their obtained clustering amplitude is slightly higher than previous surveys, as acknowledged by the authors. However, further investigation is required to ascertain the reason for the deviation. Clustering analysis was also done using the recent LoTSS observation of the HETDEX spring field (Siewert et al. 2020). The clustering analyses were produced with many flux density cut-offs and masks, and the most reliable estimate was for a flux density limit of 2 mJy at 150 MHz (or ~ 1.0 mJy at 325 MHz). The clustering amplitude estimate at 2 mJy limit for LoTSS is consistent with that obtained here within error bars. As seen from Figure 6, the clustering amplitude obtained here agrees with previous observations. The slightly higher values for the bias parameter of the AGNs for this work, compared to that of Hale et al. (2018) and Chakraborty et al. (2020), may be attributed to the different flux limits of the studies. This implies that each of these observations are probing slightly different populations of sources (with slightly different luminosities as discussed later). Nevertheless, as seen from Figure 10, the values are broadly consistent with each other.

The angular clustering amplitude for this work as shown in Figure 8 agree with previous observations, as seen in Table 3. The angular clustering of sources for this work are calculated with TreeCorr using the default values for most parameters. It has been shown in Siewert et al. (2020) that using default value of 1 for the parameter `bin_slop` gives less accurate results than for values ≤ 1 . Siewert et al. (2020) obtained the most accurate values for `bin_slop`=0. They also showed that angular clustering amplitudes deviate largely from precise values (calculated from a separate brute-force algorithm, see (Siewert et al. 2020) for details) at angular scales $\geq 1^\circ$. However, the computation times also significantly increased for `bin_slop`=0. The use of default parameters in this work might be the cause slight oscillation of the correlation function seen around the best fit curves. Nevertheless, since results obtained here are in reasonable agreement with the previous observations and owing to constraints in the available computing power, the default values have been used.

The clustering lengths and bias parameters obtained here also agree with previous studies, as evident from Table 3 and Figures 9, 10. Comparison of bias parameter with SKADS simulation Wilman et al. 2008 shows that the expected mass for dark matter haloes hosting AGNs is orders of magnitude higher than that for SFGs. This trend is consistent with previous observations (see for example Magliocchetti et al. 2017; Hale et al. 2018; Chakraborty et al. 2020). Studies on the luminosity of the AGNs and SFGs suggest that it is correlated with source clustering, and hence with the bias parameter and host halo mass (Hale et al. 2018). Using observations of high and low luminosity AGNs in the COSMOS field, Hale et al. (2018) showed that the luminosity and clustering are correlated, with the higher luminosity AGNs residing in more massive galaxies (Jarvis et al. 2001). Thus, they are hosted by more massive haloes. Again, this points to AGNs (which are in general more luminous than SFGs) being hosted by more massive haloes. However, it should also be mentioned that the two population of AGNs in Hale et al. (2018) studied are at different redshifts, with the low excitation population studied at $z \lesssim 0.65$. So it is possible that this population may evolve into higher mass haloes at higher redshifts. Moreover, some

works (for example Mendez et al. 2016) do not find any relation between clustering and luminosity. Nevertheless, following Hale et al. (2018), studies using a larger population of samples covering a large range of luminosities is required for probing the relationship with clustering.

It is also observed in Figure 10 that the bias parameter for SFGs (solid blue square) is higher than the SKADS predicted values for this population. This trend is consistent with that observed in previous studies of Hale et al. (2018) (cyan circles) and Chakraborty et al. (2020) (light magenta triangles). The trend observed in Dolley et al. (2014) (light blue diamonds) is almost similar as well. There may be two reasons that cause this variation- contamination of the SFG sample by star-burst (SB) galaxies or underestimation of halo mass for SKADS. If there exists a few SB samples in the SFG population, comparison with SKADS (blue dotted curve in Figure 10) shows that the overall value for bias (as well as r_0) will be higher than an uncontaminated sample. However, the most likely reason remains the second one, the halo mass used in the SKADS is not a correct representation, which has also been hinted at by comparing the values obtained from previous observations (for instance Dolley et al. (2014); Hale et al. (2018); Chakraborty et al. (2020)) in Figure 10. However, it is also seen from Figure 9 spatial clustering length for SFGs agrees with SKADS. The exact reason for agreement of r_0 and disagreement of $b(z)$ for SFGs in this work with SKADS is unclear, and will be investigated in detail in later works.

Analyses like the one presented here are important for fully understanding how bias scales with redshift as well as with source properties like luminosity. This is important for cosmology, since the bias relates to dark matter distribution, and is thus essential for understanding the underlying cosmological parameters that define the Universe.

It should be mentioned here that the current study also has certain limitations. Due to unknown systematics at large scales, and lack of optical matches, the entire observed field could not be utilised for this study. Additionally, the source classification is done based solely on the radio luminosity of the sources. As has already been mentioned previously, Magliocchetti et al. (2014) showed that the chances of contamination between the populations is very less using this criteria. Nonetheless, there are several other methods that can also be used to classify AGNs and SFGs in a sample (detailed in Section 2.3). Future works will present a more detailed analysis using the different multi-wavelength classification schemes available. Such multi-frequency studies, combined with the present work and similar studies with other fields will enhance the knowledge of the extragalactic sources and provide more insights into the processes governing their formation and evolution.

6 CONCLUSION

This work investigates the higher-order source statistics, namely the angular and spatial clustering of the sources detected in the Lockman Hole field. The data was observed by the legacy GMRT at 325 MHz. The details of data analysis and catalogue extraction are discussed in Mazumder et al. (2020). The initial step involved merging the multi-component sources present in the raw catalogue. The resultant catalogue was cross-matched with SDSS and HELP catalogues to identify sources with either spectroscopic or photometric redshift information. A region of radius 1.8° around the phase center was selected for optical identifications, yielding $\sim 95\%$ matches. All the sources with redshift distribution were separated into AGN and SFG populations using the criterion for radio luminosity. The

angular correlation function was determined for the combined population for separation between $36''$ to 2° . A power law fitted to this function, keeping a fixed power law index of $\gamma = 1.80$, as estimated theoretically (Peebles 1980). This gave the value of clustering amplitude $\log_{10}(A) = -2.73^{+0.11}_{-0.15}$.

The source population was further divided into AGNs and SFGs based on their radio luminosity, and clustering analyses were done for these populations as well. Using the redshift information and the clustering amplitude, spatial correlation length was determined using Limber inversion for the AGNs and SFGs. The correlation length and bias parameters have been obtained for the full sample, as well as the classified AGN and SFG population. For the full sample at $z_{\text{median}} \approx 0.78$, $r_0 = 3.50^{+0.50}_{-0.50}$ Mpc h^{-1} and $b(z) = 2.22^{+0.33}_{-0.36}$. For AGNs, the values are $r_0 = 8.30^{+0.96}_{-0.91}$ Mpc h^{-1} and $b(z) = 3.74^{+0.39}_{-0.36}$ at $z_{\text{median}} \approx 1.02$. At $z_{\text{median}} \approx 0.20$, SFGs have values $r_0 = 3.22^{+0.34}_{-0.32}$ Mpc h^{-1} and $b(z) = 1.06^{+0.10}_{-0.10}$. The clustering length for AGNs is reasonably consistent with Gilli et al. (2009) as well as Chakraborty et al. (2020). For SFGs, the values are consistent with Dolley et al. (2014).

The obtained values have also been compared with the SKADS simulation of Wilman et al. (2008). The comparative analysis suggests that the AGNs are dominated by FR-I galaxies, with host dark matter halo masses of $M_h = 5-6 \times 10^{13} h^{-1} M_\odot$. For SFGs, the estimated halo mass obtained from SKADS is lower compared to the value $\sim M_h = 3 \times 10^{12} h^{-1} M_\odot$ obtained here. The halo mass obtained here are in agreement with previous literature (Dolley et al. 2014; Hale et al. 2018; Chakraborty et al. 2020). It is worthwhile to mention that while the current classifications are based on radio luminosity for each source alone, the results are in agreement with clustering properties for populations of AGNs and SFGs in X-Ray and mid-IR surveys as well. However, there are some deviations from the predictions of the SKADS simulation. This deviation, seen in other observations as well, emphasizes the need for wider and deeper low-frequency observations. These will be able to constrain the host properties better, leading to better models formation and evolution of the different sources, and better understanding of the distribution of these populations over space and time (redshift).

The study done in this work aims to characterize the clustering and bias of an observed population of radio-selected sources, both as a combined population and as distinct classes of sources (namely AGNs and SFGs). This work is the first to report the clustering properties of radio-selected sources at 325 MHz. Thus, current data, being at a frequency with little previous clustering study, bridges the gap between low frequency and high-frequency studies. It also has the advantage of covering a wider area than many recent studies with moderately deep RMS values, thus probing a larger number of sources with fluxes at the sub-mJy level (~ 0.3 mJy). More such studies using observational data are required for constraining cosmology and probing how different source populations are influenced by their parent halos and how they evolve with time (redshift). Additionally, for sensitive observations of CD/EoR and post-EoR science, accurate and realistic models for compact source populations that comprise a significant fraction of foregrounds are required. Studies on the effect of imperfections in foreground modeling in the power spectrum estimates will require detailed observational studies of source position and flux distributions. For realistic estimates, second-order statistics like clustering also cannot be ignored. Thus many more analyses like the one done in this paper will be required for better understanding the effects of the interplay between the various cosmological parameters on the different populations of sources and putting constraints on said parameters.

Sensitive large area surveys like the MIGHTEE (Jarvis et al. 2016) with the MeerKat telescope, LoTSS (Shimwell, T. W. et al. 2017; Tasse et al. 2021; Sabater, J. et al. 2021) with the LOFAR, EMU (Norris et al. 2011, 2021) with the ASKAP, as well as those to be done with the upcoming SKA-mid telescope would provide wider as well as deeper data for doing cosmology. The current work demonstrates that even instruments like the legacy GMRT can provide reasonable data depth and coverage for cosmological observations.

ACKNOWLEDGEMENTS

AM would like to thank Indian Institute of Technology Indore for supporting this research with Teaching Assistantship. AM further acknowledges Akriti Sinha for helpful suggestions and pointing to the HELP catalogue and Sumanjit Chakraborty for helpful discussions. The authors thank the staff of GMRT for making this observation possible. GMRT is run by National Centre for Radio Astrophysics of the Tata Institute of Fundamental Research. The authors also acknowledge SDSS for the spectroscopic redshift catalogues. Funding for SDSS-III has been provided by the Alfred P. Sloan Foundation, the Participating Institutions, the National Science Foundation, and the U.S. Department of Energy Office of Science. The SDSS-III web site is <http://www.sdss3.org/>. The authors thank the anonymous reviewer for their thorough review that has helped to improve the quality of the work.

DATA AVAILABILITY

The raw data for this study is available in the GMRT archive (<https://naps.ncra.tifr.res.in/goa/data/search>). The spectroscopic redshift data is available from <https://skyserver.sdss.org/casjobs/>, and the photometric redshift data is available from <https://hedam.lam.fr/HELP/>. The PyBDSF catalogue used here (accompanying Mazumder et al. (2020)) is available on Vizier at <https://cdsarc.cds.unistra.fr/viz-bin/cat/J/MNRAS/495/4071>.

SOFTWARE

This work relies on the Python programming language (<https://www.python.org/>). The packages used here are astropy (<https://www.astropy.org/>; Astropy Collaboration et al. (2013); Price-Whelan et al. (2018)), numpy (<https://numpy.org/>), scipy (<https://www.scipy.org/>), matplotlib (<https://matplotlib.org/>), TreeCorr (<https://github.com/rmjarvis/TreeCorr>).

REFERENCES

- Abdalla F. B., et al., 2015, Cosmology from HI galaxy surveys with the SKA ([arXiv:1501.04035](https://arxiv.org/abs/1501.04035))
- Afonso J., Georgakakis A., Almeida C., Hopkins A. M., Cram L. E., Mobasher B., Sullivan M., 2005, *The Astrophysical Journal*, 624, 135
- Alam S., et al., 2021, *Phys. Rev. D*, 103, 083533
- Ali S. S., Bharadwaj S., Chengalur J. N., 2008, *MNRAS*, 385, 2166
- Allison R., et al., 2015, *Monthly Notices of the Royal Astronomical Society*, 451, 849
- Astropy Collaboration et al., 2013, *A&A*, 558, A33
- Bardeen J. M., Bond J. R., Kaiser N., Szalay A. S., 1986, *The Astrophysical Journal*, 304, 15

- Becker R. H., White R. L., Helfand D. J., 1995, *ApJ*, 450, 559
- Bell E. F., 2003, *The Astrophysical Journal*, 586, 794
- Best P. N., Heckman T. M., 2012, *Monthly Notices of the Royal Astronomical Society*, 421, 1569
- Blake C., Wall J., 2002a, *Monthly Notices of the Royal Astronomical Society*, 329, L37
- Blake C., Wall J., 2002b, *Monthly Notices of the Royal Astronomical Society*, 337, 993
- Blake C., Abdalla F., Bridle S., Rawlings S., 2004, *New Astronomy Reviews*, 48, 1063
- Blanton M. R., et al., 2017, *The Astronomical Journal*, 154, 28
- Bonaldi A., Bonato M., Galluzzi V., Harrison I., Massardi M., Kay S., De Zotti G., Brown M. L., 2018, *Monthly Notices of the Royal Astronomical Society*, 482, 2
- Bonato M., Prandoni I., De Zotti G., Brienza M., Morganti R., Vaccari M., 2020, *Monthly Notices of the Royal Astronomical Society*, 500, 22
- Bonato M., et al., 2021, The LOFAR Two-metre Sky Survey Deep fields: A new analysis of low-frequency radio luminosity as a star-formation tracer in the Lockman Hole region ([arXiv:2109.06735](https://arxiv.org/abs/2109.06735))
- Bonzini M., Padovani P., Mainieri V., Kellermann K. I., Miller N., Rosati P., Tozzi P., Vattakunnel S., 2013, *Monthly Notices of the Royal Astronomical Society*, 436, 3759
- Calistro Rivera G., et al., 2017, *Monthly Notices of the Royal Astronomical Society*, 469, 3468
- Camacho H., et al., 2019, *Monthly Notices of the Royal Astronomical Society*, 487, 3870
- Camera S., Santos M. G., Bacon D. J., Jarvis M. J., McAlpine K., Norris R. P., Raccanelli A., Röttgering H., 2012, *Monthly Notices of the Royal Astronomical Society*, 427, 2079
- Carilli C., Rawlings S., 2004, *New Astronomy Reviews*, 48, 979
- Carvalho G. C., Bernui A., Benetti M., Carvalho J. C., Alcaniz J. S., 2016, *Phys. Rev. D*, 93, 023530
- Chakraborty A., Dutta P., Datta A., Roy N., 2020, *Monthly Notices of the Royal Astronomical Society*, 494, 3392
- Chambers K. C., et al., 2019, The Pan-STARRS1 Surveys ([arXiv:1612.05560](https://arxiv.org/abs/1612.05560))
- Condon J. J., 1989, *The Astrophysical Journal*, 338, 13
- Condon J. J., Cotton W. D., Greisen E. W., Yin Q. F., Perley R. A., Taylor G. B., Broderick J. J., 1998, *The Astronomical Journal*, 115, 1693
- Cooray A., Furlanetto S. R., 2004, *ApJ*, 606, L5
- Cress C. M., Helfand D. J., Becker R. H., Gregg M. D., White R. L., 1996, *The Astrophysical Journal*, 473, 7
- Cucciati O., et al., 2012, *A&A*, 539, A31
- Davies L. J. M., et al., 2016, *Monthly Notices of the Royal Astronomical Society*, 466, 2312
- DeBoer D. R., et al., 2009, *Proceedings of the IEEE*, 97, 1507
- Delhaize J., et al., 2017, *A&A*, 602, A4
- Delvecchio I., et al., 2021, *A&A*, 647, A123
- Desjacques V., Jeong D., Schmidt F., 2018, *Physics Reports*, 733, 1
- Di Matteo T., Ciardi B., Miniati F., 2004, *MNRAS*, 355, 1053
- Dolley T., et al., 2014, *The Astrophysical Journal*, 797, 125
- Donley J. L., et al., 2012, *The Astrophysical Journal*, 748, 142
- Donoso E., Yan L., Stern D., Assef R. J., 2014, *The Astrophysical Journal*, 789, 44
- Duncan K. J., et al., 2017, *Monthly Notices of the Royal Astronomical Society*, 473, 2655
- Duncan K. J., Jarvis M. J., Brown M. J. I., Röttgering H. J. A., 2018, *Monthly Notices of the Royal Astronomical Society*, 477, 5177
- Dunlop J. S., Peacock J. A., 1990, *Monthly Notices of the Royal Astronomical Society*, 247, 19
- Dye S., et al., 2017, *Monthly Notices of the Royal Astronomical Society*, 473, 5113
- Eddington A. S., 1913, *MNRAS*, 73, 359
- Eisenstein D. J., Hu W., Tegmark M., 1999, *The Astrophysical Journal*, 518, 2
- Eisenstein D. J., et al., 2005, *The Astrophysical Journal*, 633, 560
- Eisenstein D. J., et al., 2011, *The Astronomical Journal*, 142, 72
- Fanaroff B. L., Riley J. M., 1974, *Monthly Notices of the Royal Astronomical Society*, 167, 31P
- Franzen T. M. O., Vernstrom T., Jackson C. A., Hurley-Walker N., Ekers R. D., Heald G., Seymour N., White S. V., 2019, *PASA*, 36, e004
- Galvin T. J., et al., 2020, *Monthly Notices of the Royal Astronomical Society*, 497, 2730
- Gilli R., et al., 2005, *A&A*, 430, 811
- Gilli R., et al., 2007, *A&A*, 475, 83
- Gilli R., et al., 2009, *A&A*, 494, 33
- Gürkan G., et al., 2018, *Monthly Notices of the Royal Astronomical Society*, 475, 3010
- Hale C. L., Jarvis M. J., Delvecchio I., Hatfield P. W., Novak M., Smolčić V., Zamorani G., 2018, *Monthly Notices of the Royal Astronomical Society*, 474, 4133
- Hale C. L., et al., 2019, *A&A*, 622, A4
- Hamilton A. J. S., 1993, *The Astrophysical Journal*, 417, 19
- Hao C.-N., Kennicutt R. C., Johnson B. D., Calzetti D., Dale D. A., Moustakas J., 2011, *The Astrophysical Journal*, 741, 124
- Hardcastle M. J., et al., 2016, *Monthly Notices of the Royal Astronomical Society*, 462, 1910
- Heinis S., et al., 2009, *The Astrophysical Journal*, 698, 1838
- Hildebrandt H., et al., 2016, *Monthly Notices of the Royal Astronomical Society*, 463, 635
- Huynh M. T., Jackson C. A., Norris R. P., Prandoni I., 2005, *The Astronomical Journal*, 130, 1373
- Ineson J., Croston J. H., Hardcastle M. J., Kraft R. P., Evans D. A., Jarvis M., 2015, *Monthly Notices of the Royal Astronomical Society*, 453, 2682
- Intema H. T., 2014, in *Astronomical Society of India Conference Series*. p. 469, <https://ui.adsabs.harvard.edu/abs/2014ASInC...13..469I>
- Intema H. T., van der Tol S., Cotton W. D., Cohen A. S., van Bemmell I. M., Röttgering H. J. A., 2009, *A&A*, 501, 1185
- Intema H. T., van Weeren R. J., Röttgering H. J. A., Lal D. V., 2011, *A&A*, 535, A38
- Intema H. T., Jagannathan P., Mooley K. P., Frail D. A., 2017, *A&A*, 598, A78
- Jarvis M. J., Rawlings S., Eales S., Blundell K. M., Bunker A. J., Croft S., McLure R. J., Willott C. J., 2001, *Monthly Notices of the Royal Astronomical Society*, 326, 1585
- Jarvis M., Bernstein G., Jain B., 2004, *Monthly Notices of the Royal Astronomical Society*, 352, 338
- Jarvis M. J., et al., 2010, *Monthly Notices of the Royal Astronomical Society*, 409, 92
- Jarvis M., et al., 2016, in *MeerKAT Science: On the Pathway to the SKA*. p. 6, <https://ui.adsabs.harvard.edu/abs/2016mks.confE...6J>
- Kaiser N., 1984, *The Astrophysical Journal*, 284, L9
- Kerschner M., Szapudi I., Szalay A. S., 2000, *The Astrophysical Journal*, 535, L13
- Lacey C., Cole S., 1993, *Monthly Notices of the Royal Astronomical Society*, 262, 627
- Lacey C., Cole S., 1994, *Monthly Notices of the Royal Astronomical Society*, 271, 676
- Landy S. D., Szalay A. S., 1993, *The Astrophysical Journal*, 412, 64
- Lawrence A., et al., 2007, *Monthly Notices of the Royal Astronomical Society*, 379, 1599
- Lewis J. R., Bunclark P. S., Irwin M. J., McMahon R. G., Walton N. A., 2000, in *Astronomical Data Analysis Software and Systems IX*. p. 415, <https://ui.adsabs.harvard.edu/abs/2000ASPC..216..415L>
- Limber D. N., 1953, *The Astrophysical Journal*, 117, 134
- Lindsay S. N., et al., 2014, *Monthly Notices of the Royal Astronomical Society*, 440, 1527
- Ling E. N., Frenk C. S., Barrow J. D., 1986, *Monthly Notices of the Royal Astronomical Society*, 223, 21P
- Magliocchetti M., Maddox S. J., Lahav O., Wall J. V., 1998, *Monthly Notices of the Royal Astronomical Society*, 300, 257
- Magliocchetti M., et al., 2002, *Monthly Notices of the Royal Astronomical Society*, 333, 100

- Magliocchetti M., et al., 2004, *Monthly Notices of the Royal Astronomical Society*, 350, 1485
- Magliocchetti M., et al., 2013, *Monthly Notices of the Royal Astronomical Society*, 433, 127
- Magliocchetti M., et al., 2014, *Monthly Notices of the Royal Astronomical Society*, 442, 682
- Magliocchetti M., Lutz D., Santini P., Salvato M., Popesso P., Berta S., Pozzi F., 2015, *Monthly Notices of the Royal Astronomical Society*, 456, 431
- Magliocchetti M., Popesso P., Brusa M., Salvato M., Laigle C., McCracken H. J., Ilbert O., 2017, *Monthly Notices of the Royal Astronomical Society*, 464, 3271
- Magnelli B., et al., 2015, *A&A*, 573, A45
- Matteo T. D., Perna R., Abel T., Rees M. J., 2002, *ApJ*, 564, 576
- Mauduit J.-C., et al., 2012, *Publications of the Astronomical Society of the Pacific*, 124, 714
- Mazumder A., Chakraborty A., Datta A., Choudhuri S., Roy N., Wadadekar Y., Ishwara-Chandra C. H., 2020, *Monthly Notices of the Royal Astronomical Society*, 495, 4071
- McAlpine K., Jarvis M. J., Bonfield D. G., 2013, *Monthly Notices of the Royal Astronomical Society*, 436, 1084
- Mendez A. J., et al., 2016, *The Astrophysical Journal*, 821, 55
- Mignano, A. Prandoni, I. Gregorini, L. Parma, P. de Ruiter, H. R. Wieringa, M. H. Vettolani, G. Ekers, R. D. 2008, *A&A*, 477, 459
- Mo H., van den Bosch F., White S., 2010, *Galaxy Formation and Evolution*. Cambridge University Press, Cambridge, <https://www.cambridge.org/core/books/galaxy-formation-and-evolution/E236D9F26B797202BCA28637BF17E75F>
- Mohan N., Rafferty D., 2015, PyBDSF: Python Blob Detection and Source Finder (ascl:1502.007)
- Muzzin A., Wilson G., Collaboration S., 2007, in American Astronomical Society Meeting Abstracts. p. 78.05, <https://ui.adsabs.harvard.edu/abs/2007AAS...211.7805M>
- Norberg P., et al., 2001, *Monthly Notices of the Royal Astronomical Society*, 328, 64
- Norris R. P., et al., 2011, *Publications of the Astronomical Society of Australia*, 28, 215
- Norris R. P., et al., 2013, *Publications of the Astronomical Society of Australia*, 30, e020
- Norris R. P., et al., 2021, *Publications of the Astronomical Society of Australia*, 38, e046
- Ocran E. F., Taylor A. R., Vaccari M., Ishwara-Chandra C. H., Prandoni I., Prescott M., Mancuso C., 2019, *Monthly Notices of the Royal Astronomical Society*, 491, 5911
- Ocran E. F., Taylor A. R., Vaccari M., Ishwara-Chandra C. H., Prandoni I., Prescott M., Mancuso C., 2020, *Monthly Notices of the Royal Astronomical Society*, 500, 4685
- Oort M. J. A., 1987, PhD thesis, Leiden Observatory, <https://ui.adsabs.harvard.edu/abs/1987PhDT.....400>
- Overzier R. A., Röttgering H. J. A., Rengelink R. B., Wilman R. J., 2003, *A&A*, 405, 53
- Padovani P., 2016, *The Astronomy and Astrophysics Review*, 24, 13
- Padovani P., Bonzini M., Kellermann K. I., Miller N., Mainieri V., Tozzi P., 2015, *Monthly Notices of the Royal Astronomical Society*, 452, 1263
- Peacock J. A., Smith R. E., 2000, *Monthly Notices of the Royal Astronomical Society*, 318, 1144
- Peacock J. A., et al., 2001, *Nature*, 410, 169
- Peebles P. J. E., 1980, *The large-scale structure of the universe*. Princeton University Press
- Percival W. J., et al., 2001, *Monthly Notices of the Royal Astronomical Society*, 327, 1297
- Planck Collaboration et al., 2014, *A&A*, 571, A17
- Planck Collaboration et al., 2019, *A&A*
- Prandoni I., Guglielmino G., Morganti R., Vaccari M., Maini A., Röttgering H. J. A., Jarvis M. J., Garrett M. A., 2018, *MNRAS*, 481, 4548
- Prescott M., et al., 2016, *Monthly Notices of the Royal Astronomical Society*, 457, 730
- Press W. H., Schechter P., 1974, *The Astrophysical Journal*, 187, 425
- Price-Whelan A. M., et al., 2018, *AJ*, 156, 123
- Raccanelli A., et al., 2012, *Monthly Notices of the Royal Astronomical Society*, 424, 801
- Raccanelli A., et al., 2015, *Journal of Cosmology and Astroparticle Physics*, 2015, 042
- Rana S., Bagla J. S., 2019, *Monthly Notices of the Royal Astronomical Society*, 485, 5891
- Ross N. P., et al., 2007, *Monthly Notices of the Royal Astronomical Society*, 381, 573
- Rowan-Robinson M., et al., 2008, *Monthly Notices of the Royal Astronomical Society*, 386, 697
- Rowan-Robinson M., Gonzalez-Solares E., Vaccari M., Marchetti L., 2012, *Monthly Notices of the Royal Astronomical Society*, 428, 1958
- Sabater, J. et al., 2021, *A&A*, 648, A2
- Salazar-Albornoz S., et al., 2017, *Monthly Notices of the Royal Astronomical Society*, 468, 2938
- Saxena A., Röttgering H. J. A., Rigby E. E., 2017, *Monthly Notices of the Royal Astronomical Society*, 469, 4083
- Seldner M., Peebles P. J. E., 1981, *Monthly Notices of the Royal Astronomical Society*, 194, 251
- Seljak U. c. v., 2009, *Phys. Rev. Lett.*, 102, 021302
- Seymour N., et al., 2008, *Monthly Notices of the Royal Astronomical Society*, 386, 1695
- Shaver P. A., Pierre M., 1989, *Astronomy and Astrophysics*, 220, 35
- Shaver P. A., Windhorst R. A., Madau P., de Bruyn A. G., 1999, *A&A*, 345, 380
- Sheth R. K., Tormen G., 1999, *Monthly Notices of the Royal Astronomical Society*, 308, 119
- Shi F., et al., 2016, *The Astrophysical Journal*, 833, 241
- Shimwell, T. W. et al., 2017, *A&A*, 598, A104
- Shimwell, T. W. et al., 2019, *A&A*, 622, A1
- Shirley R., et al., 2019, *Monthly Notices of the Royal Astronomical Society*, 490, 634
- Siewert T. M., et al., 2020, *A&A*, 643, A100
- Simpson C., et al., 2006, *Monthly Notices of the Royal Astronomical Society*, 372, 741
- Singh V., et al., 2014, *A&A*, 569, A52
- Smolčić V., et al., 2008, *The Astrophysical Journal Supplement Series*, 177, 14
- Smolčić V., et al., 2017, *A&A*, 602, A6
- Starikova S., Berta S., Franceschini A., Marchetti L., Rodighiero G., Vaccari M., Vikhlinin A., 2012, *The Astrophysical Journal*, 751, 126
- Swarup G., Ananthakrishnan S., Kapahi V. K., Rao A. P., Subrahmanya C. R., Kulkarni V. K., 1991, *Current Science*, Vol. 60, NO.2/JAN25, P. 95, 1991, 60, 95
- Szokoly G. P., et al., 2004, *The Astrophysical Journal Supplement Series*, 155, 271
- Tasse C., et al., 2021, *A&A*, 648, A1
- Tiwari P., Ghosh S., Jain P., 2019, *The Astrophysical Journal*, 887, 175
- Trott C. M., et al., 2016, *ApJ*, 818, 139
- Vernstrom T., Scott D., Wall J. V., Condon J. J., Cotton W. D., Kellermann K. I., Perley R. A., 2016, *Monthly Notices of the Royal Astronomical Society*, 462, 2934
- Wang Y., Brunner R. J., Dolence J. C., 2013, *Monthly Notices of the Royal Astronomical Society*, 432, 1961
- Williams, W. L. et al., 2019, *A&A*, 622, A2
- Williams W. L., Intema H. T., Röttgering H. J. A., 2013, *A&A*, 549, A55
- Williams W. L., et al., 2018, *Monthly Notices of the Royal Astronomical Society*, 475, 3429
- Wilman R. J., et al., 2008, *Monthly Notices of the Royal Astronomical Society*, 388, 1335
- York D. G., et al., 2000, *The Astronomical Journal*, 120, 1579
- de Simoni F., et al., 2013, *Monthly Notices of the Royal Astronomical Society*, 435, 3017
- van Haarlem, M. P. et al., 2013, *A&A*, 556, A2

This paper has been typeset from a \LaTeX file prepared by the author.